Icarus 354 (2021) 114059

Contents lists available at ScienceDirect

Icarus

journal homepage: www.elsevier.com/locate/icarus

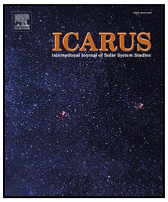

Research Paper

The Mars Dust Activity Database (MDAD): A comprehensive statistical study of dust storm sequences

Michael Battalio*, Huiqun Wang

Smithsonian Astrophysical Observatory, Harvard-Smithsonian Center for Astrophysics, 60 Garden Street, MS 50, Cambridge, MA 02138, United States of America

ARTICLE INFO

Keywords:
Atmospheres
Dynamics
Mars
Climate

ABSTRACT

A comprehensive Mars Dust Activity Database (MDAD) over 8 Mars years (MY 24, $L_s = 150°$ to MY 32, $L_s = 171°$) is compiled from Mars Daily Global Maps. A total of 14,974 dust storm instances are cataloged with area $>10^5$ km^2 that are visually distinguishable from the surface. A dust storm instance is identified as a dust storm member over multiple sols if storm movement can be tracked. Dust storm sequences are collections of members that have a coherent trajectory from their origination areas over three or more sols. There are 228 sequences, with 125 originating in the northern hemisphere. Sequences primarily originate in Acidalia, Utopia, and Arcadia Planitiae in the northern hemisphere and Aonia–Solis–Valles Marineris and Hellas Basin in the southern hemisphere. Many northern hemisphere originating sequences flush into the southern hemisphere. The primary season for non-global dust events occurs during $L_s = 140°– 250°$, with secondary seasons in $L_s = 300°– 360°$ in the northern hemisphere and $L_s = 10°– 70°$ in the southern hemisphere. Sequences are classified into three types. Main Member sequences have one dominant member; Continuous Development sequences have many smaller members; and Sequential Redevelopment sequences have repeating, medium-sized members. “Major” sequences have a maximum area $>10^7$ km^2, influence the zonal-mean global opacity, and exhibit flushing behavior. Major sequences occur over a narrower temporal range and are distinguished from other sequences by the larger size and duration distributions of their constituent members. Major sequences have unique antecedent conditions, with steadily increasing dust storm area in the 6 preceding sols that is significantly distinct from conditions preceding minor sequences.

1. Introduction

Dust storms are one of the defining features of the Martian atmosphere and range from microscale dust devils to global dust events (GDEs). Dust greatly impacts the thermal structure of the atmosphere (Kass et al., 2016) and its circulation (Barnes et al., 2017). Thus, dust activity is inexorably connected to the Martian climate through dynamical-radiative feedbacks (Haberle et al., 1993; Toigo et al., 2018) and so is important for spacecraft operations both on the surface and during the Entry-Descent-Landing stage. Observational climatologies, in particular, are important for guiding modeling efforts of the Martian atmosphere in the planning stages of missions.

Medium to large dust events usually occur in the second half of the Mars year during northern hemisphere fall and winter ($L_s = 150°–360°$) (Martin and Zurek, 1993; Cantor et al., 2001; Wang, 2007; Guzewich et al., 2015, 2017) and grow by aggregation of smaller dust storms from multiple, smaller lifting centers (Cantor et al., 2001; Strausberg et al., 2005; Cantor, 2007; Wang and Richardson, 2015). Most dust activity is confined to the edge of the polar ice caps (Cantor et al., 2001; Guzewich et al., 2015) and has traditionally been grouped by size. Martin and Zurek (1993) categorized dust events with a long axis of greater than 2000 km as non-local dust storms. Cantor et al. (2001) deemed dust storms with areas greater than 1.6×10^6 km^2 and durations of greater than 3 Mars days (sols) as “regional” events. Wang and Richardson (2015) identified all dust activity between 1999 and 2011 larger than 10^6 km^2.

Regional events are typically associated with baroclinic wave activity (Hinson et al., 2012; Haberle et al., 2018; Battalio and Wang, 2019, 2020) and so exhibit the same temporal variations, with a minimum during solstices (Mooring and Wilson, 2015; Lewis et al., 2016; Mulholland et al., 2016; Battalio et al., 2018). Accordingly, baroclinic activity and regional dust events occur in defined storm tracks in the northern and southern midlatitudes, especially through Acidalia, Utopia, and Arcadia Planitae in the north (Hollingsworth and Barnes, 1996; Wang and Richardson, 2015) and the Aonia–Solis–Valles Marineris area in

---

[*] Correspondence to: Department of Earth and Planetary Sciences, Yale University, 210 Whitney Ave., New Haven, CT 06511, United States of America
E-mail address: michael@battalio.com (M. Battalio).

https://doi.org/10.1016/j.icarus.2020.114059
Received 25 February 2020; Received in revised form 10 August 2020; Accepted 12 August 2020
Available online 21 August 2020
0019-1035/© 2020 Elsevier Inc. All rights reserved.

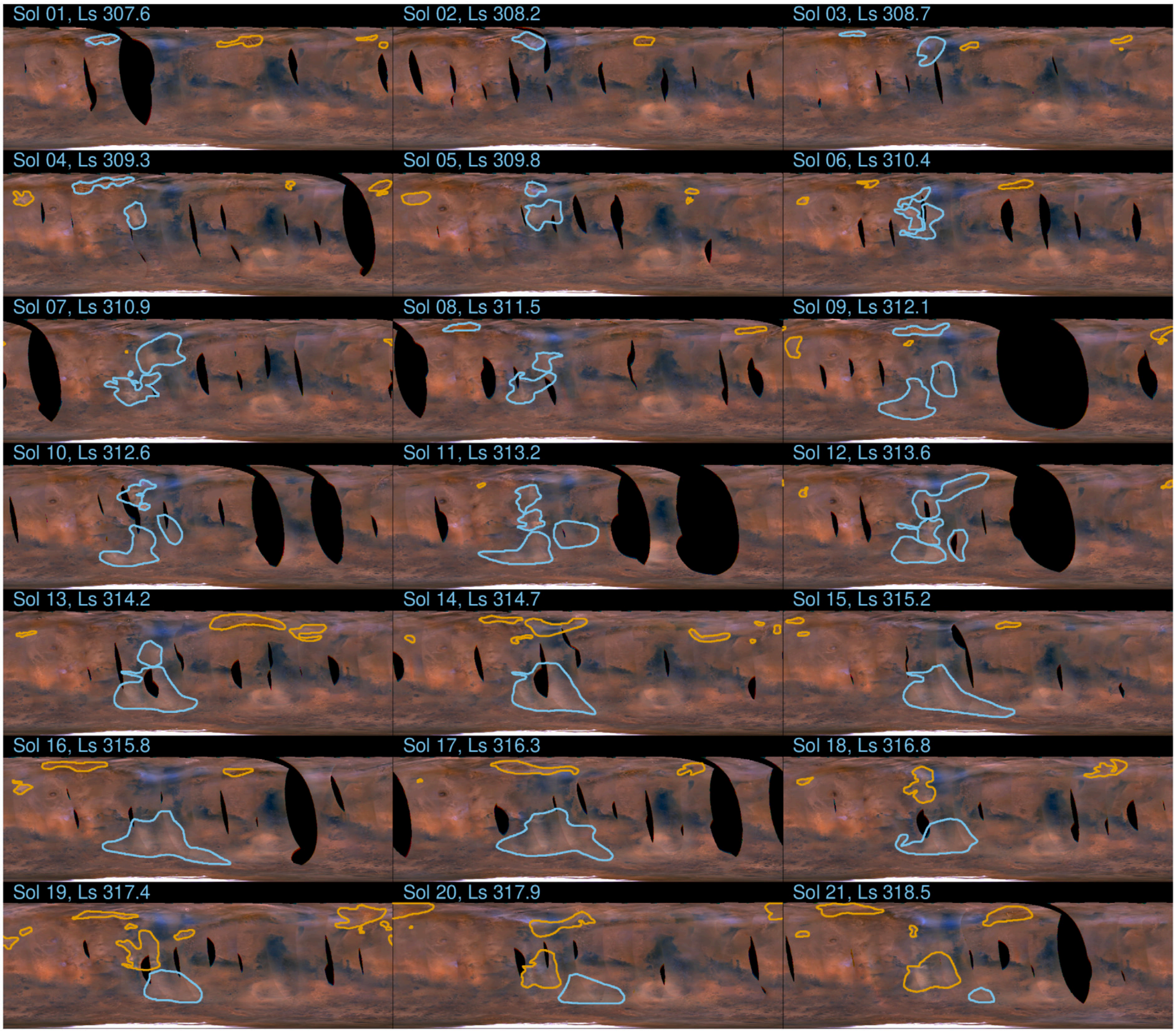

Fig. 1. Progression of a large dust storm sequence from the MDAD in MY 30 during L_s = 307.6°–318.5°. Dust storm members associated with the dust storm sequence are outlined in light blue; other dust storms members are outlined in gold. The sol number of the event and the L_s are labeled at the top left of each panel. (For interpretation of the references to color in this figure legend, the reader is referred to the web version of this article.)

the south (Battalio et al., 2018; Battalio and Wang, 2019). The largest yearly events have specific impacts on the global temperature structure and are designated A, B, and C events (Kass et al., 2016). A and C events are usually the result of flushing dust storms (Wang et al., 2013) that are triggered by baroclinic waves in the northern hemisphere and cross the equator to grow in the southern hemisphere (Battalio and Wang, 2020). B events are usually confined to the southern hemisphere polar region.

While previous efforts have mined the Mars Daily Global Maps for dust storm climatologies (e.g., Wang and Ingersoll, 2002; Wang et al., 2003; Wang and Richardson, 2015; Guzewich et al., 2015, 2017; Kulowski et al., 2017), few have done so by comprehensively tracking each dust storm member. This work follows individual dust storm instances over multiple sols, improves the temporal and spatial coverage of the dust storm climatology, and investigates the difference between organized and non-organized dust storm events. A long-term climatology of all distinct dust activity over 8 Mars years (MY) (1999–2014) at all visually identifiable sizes (10^5 km^2 and larger) is compiled. Multi-sol dust events are tracked, and organized activity with a duration of more than 3 sols is categorized. The results are presented in three parts: (1) the climatologies of dust storm activity are presented, refining and updating Wang and Richardson (2015); (2) the development of large, organized dust events is categorized by development type; and (3) the precursor conditions favorable for particularly impactful dust storms are identified.

2. Methods

This work describes and interrogates the Mars Dust Activity Database (MDAD) to characterize recent dust storm activity. The MDAD is compiled using Mars Daily Global Maps (MDGMs) from MY 24 to MY 32. The MDGM database includes maps from the Mars Global Surveyor (MGS) Mars Orbiter Camera (MOC) from MY 24 L_s = 150° to MY 28 L_s = 121° and the Mars Reconnaissance Orbiter (MRO) Mars Color Imager (MARCI) from MY 28 L_s = 133° to MY 32 L_s = 171°. Each MDGM is composed of up to 13 global image swaths taken over about one sol. The image swaths are stitched together to form a 0.1° longitude × 0.1° latitude grid map. Each MRO MDGM covers 90°N–90°S (Wang and Richardson, 2015), and each MGS MDGM is separated into a north polar (45°N–90°N), a south polar (45°S–90°S), a nonpolar (60°S–60°N) map (Wang and Ingersoll, 2002). The nonpolar MGS MOC and the Version 2 MRO MARCI MDGMs are used in this study.

Fig. 1 illustrates the type of data contained in the MDAD. Each panel is a MARCI MDGM from MY 30, with the sol number and the L_s listed on the top left. Black areas are due to polar night or missing data. Individual dust storm instances with well-defined boundaries are outlined manually in MDGMs. In Fig. 1, storms associated with a particular organized event are enclosed in light blue, and other storms are enclosed in gold. In the event of missing data, the edge of the dust storm is extrapolated across the missing data area (e.g., Fig. 1, Sol 14). Each storm instance is identified by a member ID that can be carried across sols if the motion of the dust storm instance is possible based on the distance traversed over consecutive sols and the member's previous translation rate. For example, the dust storm instances encircled in light blue in Fig. 1, Sols 1 & 2 are given the same member ID. Thus, a dust storm member consists of a dust storm instance occurring on one or more consecutive sols. If a member cannot be tracked due to missing data, a new member ID is assigned. Different members can merge into a single member. Conversely, a single member can split into multiple members. Therefore, in this paper, a "dust storm instance" refers to an enclosed dust region on a single sol, but a "dust storm member" is the whole multi-sol lifetime of a dust storm instance, which may be only one sol in duration. "Dust storm activity" refers to all of the dust storm instances on a given sol.

A confidence level of 25, 50, 75, or 100 is subjectively assigned to each identified dust storm instance to describe the accuracy of boundaries, with 25 being the least confident. A confidence level of 100 means that the entire perimeter of the dust storm instance is distinct against the surface so that the edge has an error on the order of a few pixels (~0.5°). Any instance suffering from missing data has at most a confidence level of 75 (e.g., the instance circled in light blue on Sol 18 in Fig. 1) and is further labeled with a "missing data" flag in the MDAD. A confidence level of 25 means some or all of the perimeter of the dust storm instance has nebulous boundaries that cannot be exactly discerned from the background within several degrees of latitude/longitude. The confidence level is also used to discern how distinct a dust storm instance is from the background opacity. For the purposes of this study, an individual dust storm instance loses its distinctiveness and ceases to be identified when its edges cannot be determined against surface albedo features or if dust of a similar opacity covers more than half of a latitude circle. This definition is particularly important in the categorization of the GDEs in MYs 25 and 28, where only minor changes in opacity might indicate areas of active lifting versus transported dust. For example, the dust storm instance encircled in light blue on Sol 1 of Fig. 1 has a confidence level of 100, as the boundaries of the dust storm instance are distinct, but the storm on Sol 20 has a less distinctive boundary and is given a confidence level of 50. In this study, storm instances with a confidence level of 50 or greater are included.

Large-scale, organized dust events are called dust storm "sequences" (Wang and Richardson, 2015). Sequences are collections of one or more dust storm members that follow a general trajectory (Battalio and Wang, 2019, 2020). Sequences defined here have a lifetime of 3 or more sols, which is longer than the duration of the individual members of the sequences, except in the case of sequences with only one dust storm member. In Fig. 1, the sequence is the collection of all individual dust instances enclosed in light blue. Dust storms instances not associated with the given sequence are shown in gold—many of which belong to another sequence (Supplemental Fig. 1) immediately following the one depicted in Fig. 1. Sequences are identified with a sequence ID that allows for the organized dust events to be distinguished from other dust storm activity. A post-processing algorithm is used to calculate the area and centroid of each dust storm instance, the durations of dust storm members, and organize dust storm sequences. The MDAD is available at the Harvard Dataverse (doi: 10.7910/DVN/F8R2JX).

3. Results

We divide the analysis into three parts. The first section describes the aggregate statistics of dust storm activity in the MDAD—both that organized into sequences and not. The second section investigates more closely the nature of the sequences in the MDAD by classifying sequences into three groups, and the final section defines sequences into "major" and "minor" types.

3.1. The mars dust activity database

The MDAD contains 7,927 dust storm members, composed of 14,974 individual dust storm instances. The average number of dust storm instances is 1,898 per year. A total of 228 sequences are cataloged, of which 125 originate in the northern hemisphere, and 103 originate in the southern hemisphere.

3.1.1. Temporal distribution

The multi-year cycle of dust storm activity is shown in Fig. 2. Each panel is one Mars year, beginning with MY 24 and ending with MY 32. The colored contours in shades of green are the 9.3 μm zonal-mean dust optical depth scaled to 610 Pa (Montabone et al., 2015). Horizontal dashed lines bound the periods of MGS MOC collected data, and the vertical dashed lines in MY 24 and 32 indicate the start and stop times of the MDAD. Hatching denotes periods of missing data. Individual dust storm instances from the MDAD are shown with circles scaled by their respective areas. Vertical lines through each circle show the latitudinal extent of the dust instance. Dust storm instances belonging to a dust storm sequence are shown in blue (minor sequences) or gold (major sequences, Section 3.3), and all other dust storm instances are shown in black.

The general temporal pattern of dust storm instances is similar across all nine years; dust activity usually follows the edge of the polar ice caps, in accordance with the results of Guzewich et al. (2017) and Battalio and Wang (2019). The largest amounts of activity occur during fall and winter in both hemispheres. Reduced amounts of dust storm activity during the solstices correspond to solstitial pauses of transient eddies in the lower atmosphere (Lewis et al., 2016). In aggregate, the unorganized instances (indicated by black circles in Fig. 2) do not exhibit much interannual variability in that the latitudes, coverage, timing, and number of instances do not vary much from one season and latitude to another. However, the detail of individual dust storm instances shows considerable variability in a specific latitude and time of year.

Organized dust storm sequences (shown in blue and gold in Fig. 2) are most prevalent in the northern hemisphere during fall and winter. Some remain along the periphery of the polar vortex and confined to the middle and high latitudes, but many flush towards the equator. This behavior is particularly notable from the northern hemisphere to the southern between L_s = 180°–240° and L_s = 300°–350°. However, there are storm tracks in the southern hemisphere that do flush northwards, like the Aonia–Solis–Valles Marineris storm track (Battalio and Wang, 2019) during L_s = 20°–60° and L_s = 120°–180°. These organized episodes of dust activity occur in clusters, with occasional periods of tens of L_s without any organized systems. Battalio and Wang (2020) suggested that this clustering can be the result of dust events being self-limiting by stabilizing the atmosphere to baroclinic waves.

Within the catalog of organized dust activity, there are repeated instances of very large dust events that correspond in Fig. 2 to pronounced increases of background dust opacity as compared to the annual dust cycle. Many of these larger events have been described in Kass et al. (2016) according to their impact on the atmospheric temperatures in MCS retrievals and in Montabone et al. (2015) in terms of their column dust optical depth as the pre-winter solstice (with respect to the northern hemisphere) "A", near-solstice "B", and post-solstice "C" dust storms. The interannual variability of these larger events is more pronounced compared to the sequences that are smaller in area and duration and is especially apparent compared to the unorganized, non-sequence dust members. The size and timing of these major events varies across years, with some occurrences of the B or C storms being nearly absent (e.g., the C event in MYs 24, 25, and 28, Battalio and Wang, 2020). The most obvious sources of interannual variability in the MDAD are the GDEs at L_s = 185°–210° in MY 25 and L_s = 265°–290° in MY 28. They have their largest lifting in the southern hemisphere

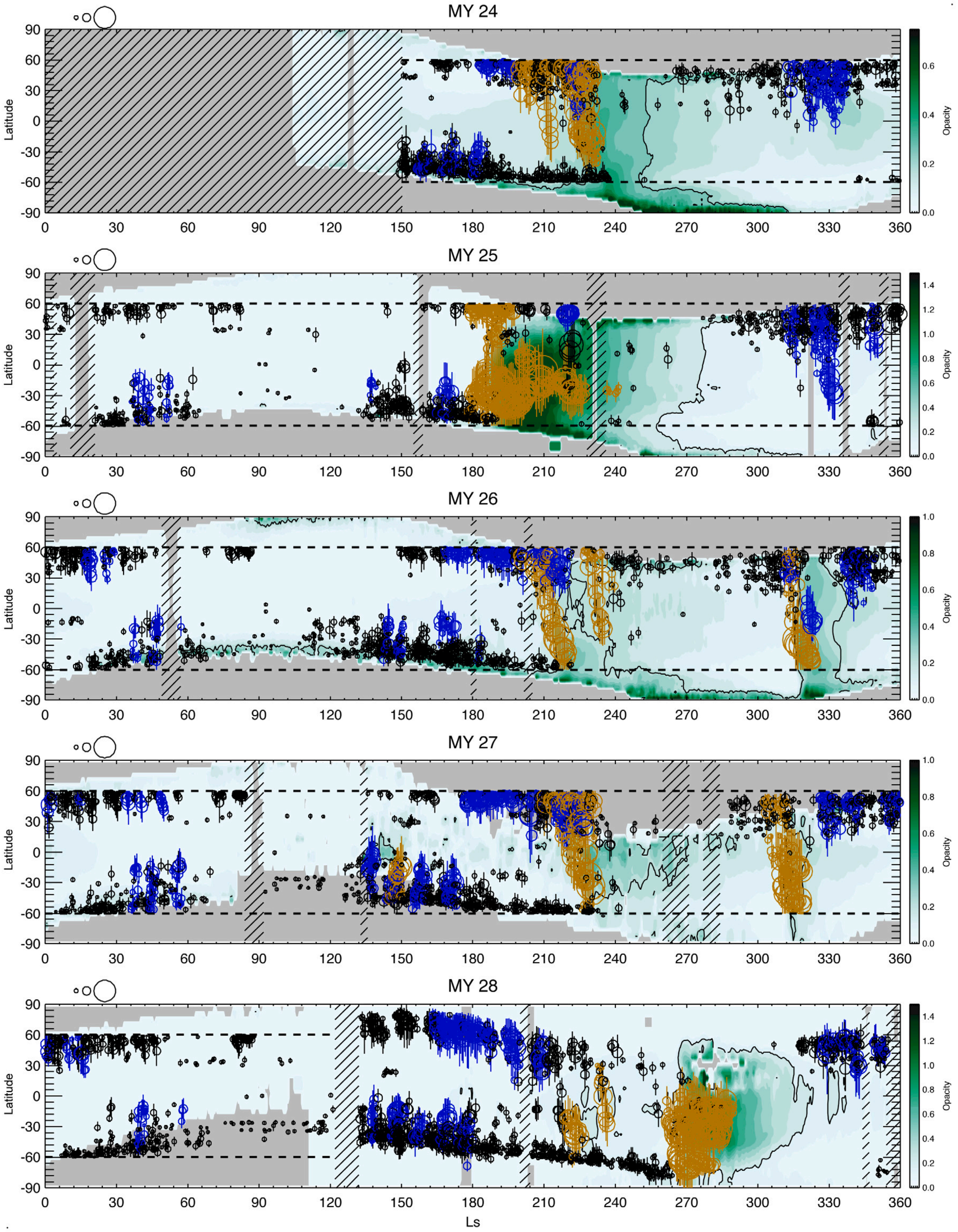

Fig. 2. Distribution of dust storm instances for each year. Circles indicate centroid latitudes and L_s of dust storm instances and are scaled by dust storm instance sizes. Legends at the top of each panel indicate the sizes of storms: 10^6, 5×10^6, and 10^7 km^2. The vertical lines through each circle indicate the latitudinal extent of each instance. Dust storm instances associated with sequences are colored blue, major sequences are colored gold (Section 3.3), and other instances are black. Periods of missing data are shown with hatching. Years from the MGS MOC MDGMs are indicated with dashed lines at 60°N/S. The vertical dashed line in MY 24 and MY 32 indicates the start/end of the MDAD. Filled green contours, with the 0.3 contour in black, indicate the 9.3 μm zonal-mean dust opacity (scaled to 610 Pa) of Montabone et al. (2015). (For interpretation of the references to color in this figure legend, the reader is referred to the web version of this article.)

and have been discussed elsewhere (Strausberg et al., 2005; Cantor, 2007).

We use the long record of the MDAD to examine local timescales of dust storm impacts, noting that background opacity is not considered. Fig. 3 shows the average duration of dust storm obscuration at a particular point (a) and the amount of time between dust storm occurrence (b). The maps were generated by binning all points to 1° × 1°, stepping forward in time from the beginning of the MDAD until a sol was found

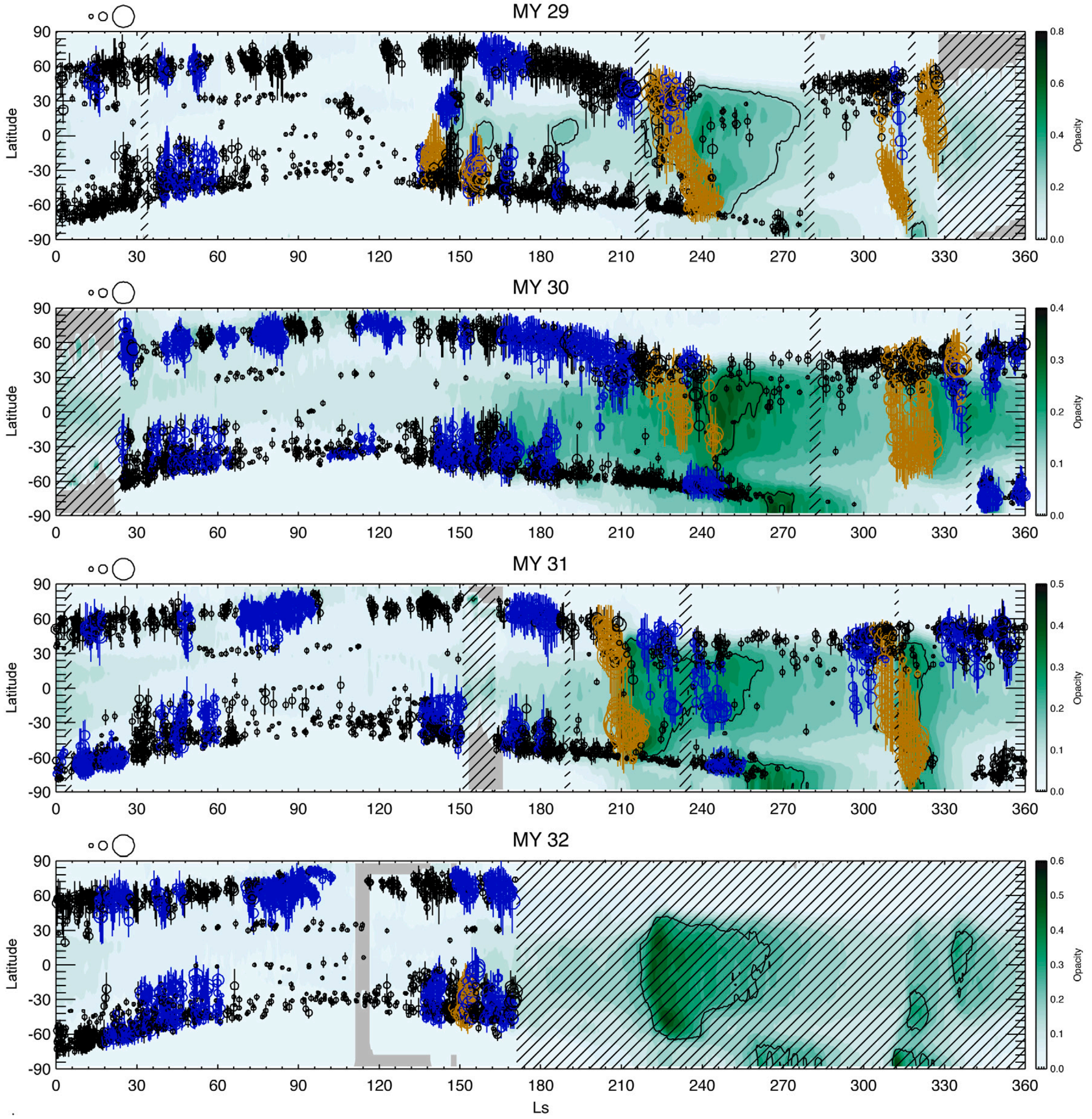

Fig. 2. (*continued*).

where an individual pixel was dusty. Once a dusty pixel was indicated, the duration that the pixel remained obscured by a dust storm instance was recorded. The procedure was repeated for the entirety of the dataset. Points in gray in Fig. 3 had too few incidences of dust storm activity (<5) to perform the calculation. For the dust storm duration, the lifting regions of the GDEs in the southern hemisphere stand out, but there are local maxima in Utopia and Acidalia Planitiae and in Xanthe Terra. The recurrence interval along the equator, except through the Acidalia channel, is uniformly large, but the recurrence interval along 60°N/S, within the baroclinic storm tracks (Battalio et al., 2016, 2018), is much shorter. Perhaps most striking is the tight gradient in recurrence interval along the northern boundaries of Arabia Terra and the Tharsis Plateau, where only a few degrees of latitude separates the dust storm tracks from the relatively clear conditions of the equatorial highlands. These results are somewhat insensitive to the confidence level—thus the distinctiveness of dust instance boundaries—chosen, as using a confidence level of 25 instead of 50 yields an average change in dusty duration of only 0.098 sols.

3.1.2. *Spatial distribution*

Fig. 4 shows the spatial distribution of all dust storm instances in the MDAD. For each $0.1° \times 0.1°$ MDGM pixel, the number of sols where the pixel is dusty was divided by the total number of sols of available data for that pixel. The top panel shows the frequency of dust events in MY 24–28 during the MOC MDGM era and extends only as far poleward as 60°N/S (indicated with hatching). The bottom panel shows the frequency of dust events from MY 29–32 during the MARCI era and extends to the poles. The maximum frequency of dust storm instances is approximately 18% and occurs in only a limited area within Acidalia Planitia. There are two other regions of relatively high dust storm instance frequency in Utopia Planitia and Xanthe Terra, between 12 and 15% frequency. Two further local maxima with around 10% frequency are in Arcadia Planitia and along the northern flank of Hellas. It will be shown later that these regions are populated with large numbers of dust storm sequences. There are also multiple local maxima throughout the southern highlands between 8 and 10% frequency. The equatorial regions have reduced frequency of dust activity in general, but notably, there are three local minima in dust storm instance frequency along the equator: Tharsis, Arabia Terra, and Elysium Planitia. The minor differences in the amplitude of the individual maxima in the MOC era (top) and MARCI era (bottom) are not necessarily reflective of trends in dust activity, as the MOC era includes only the second half of MY 24

a) Average Dusty Duration

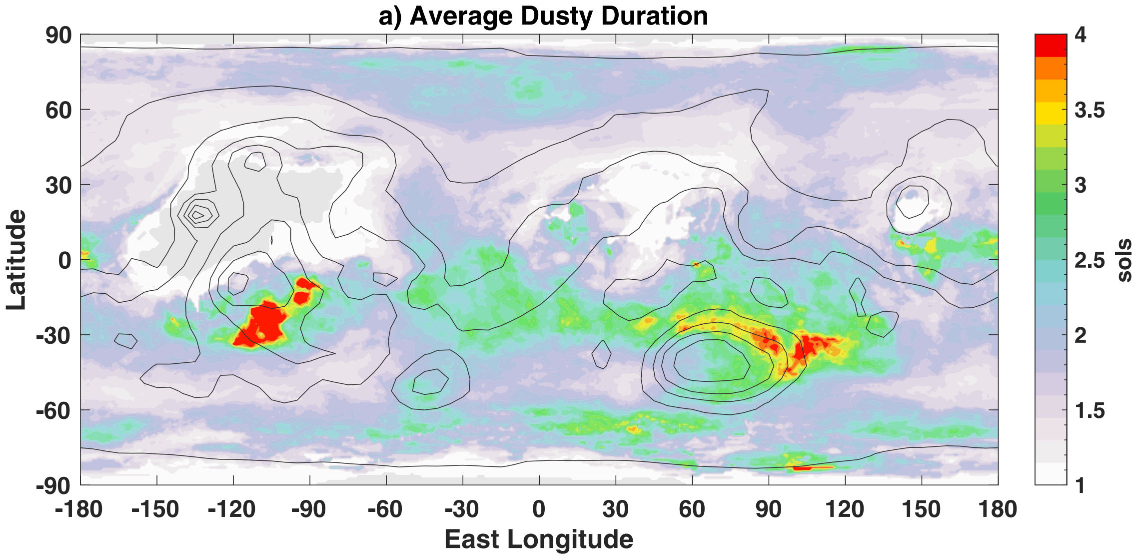

b) Average Storm Recurrence Interval

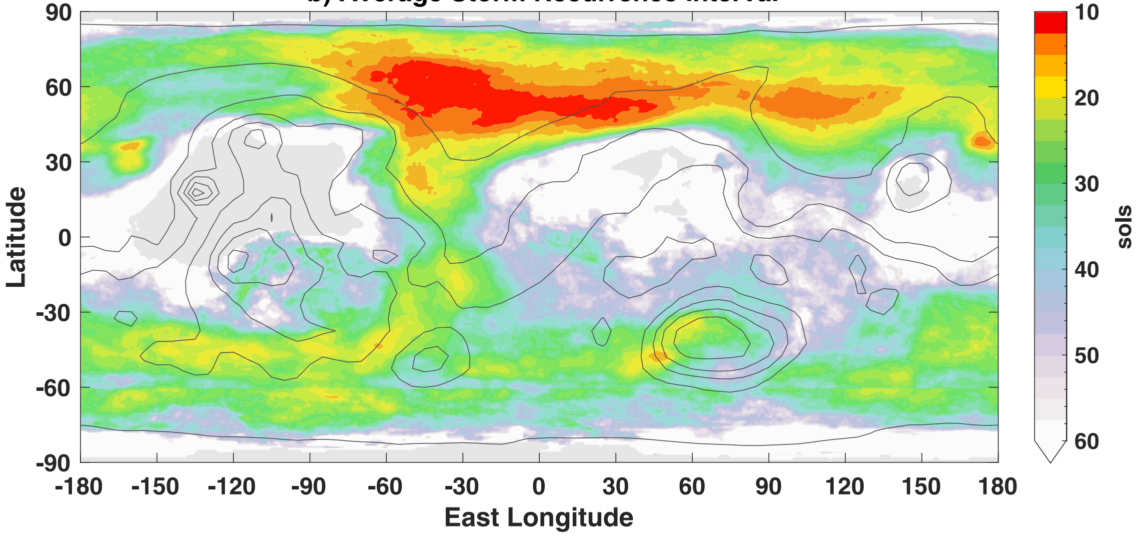

Fig. 3. Average duration of dust storm coverage for each 1° × 1° area from the MDAD (a) and the average recurrence interval for dust storm activity (b). Pixels with fewer than 5 dust storm instances are masked in light gray. Topography is shown in black contours every 2000 m. (For interpretation of the references to color in this figure legend, the reader is referred to the web version of this article.)

that is typically the dusty season, and the MARCI era includes the first half of MY 32 (Fig. 2).

However, as was shown in Fig. 2, there is some interannual variability. Supplemental Figure 2 shows the spatial distribution for each year individually, generated in the same way as Fig. 4. Most years have a spatial distribution of dust activity that is similar to the total frequency in Fig. 4; however, there are notable exceptions. The lifting center in Solis Planum from the GDE of MY 25 is the most obvious exception, but each year has some minor differences. For example, MY 26 has reduced activity in the Aonia–Solis–Valles Marineris track (Battalio and Wang, 2019). MY 30 has a more pronounced Utopia storm area, with a reduced maximum in Acidalia, and MY 31 has reduced activity overall. Despite these differences, there is a consistent spatial pattern of dust activity across all 9 years.

3.1.3. Sequence versus non-sequence storm instances

As noted in Fig. 2, organized sequences of dust storms are common from fall to spring of each hemisphere. All 228 sequences, including their timing, maximum size, duration, type, origination region, and number of members are listed in Supplemental Table 1. Fig. 5 shows the distribution of dust storm instances that are part of a sequence (top) and not part of a sequence (bottom). Each circle indicates the position of the centroid of an individual instance on a particular sol. Symbol sizes are proportional to the area of the indicated instance. As reflected in Figs. 2 and 4, most activity is confined to a band between 30–70°N, with some dust storm instances flushing towards the equator in specific longitudinal bands, including 90–130°E, 0–60°W, and around 180°E. It is clear in the top panel of Fig. 5 that most of the cross-equatorial flushing happens through Acidalia by sequence members; relatively few non-sequence instances occur near the equator. Additionally, the band of sequence versus non-sequence dust instances is shifted slightly equatorward in the southern hemisphere to be more aligned with 30°S, reflective of the flushing nature of dust activity, particularly in the Aonia–Solis–Valles Marineris track.

Several peaks of non-sequence activity are not duplicated within sequences around 30°N and 30°S. These each align with topographic features. At 30°S, between 70° and 100°W, the concentration of dust storms instances coincides with the southern ridge of Solis Planum

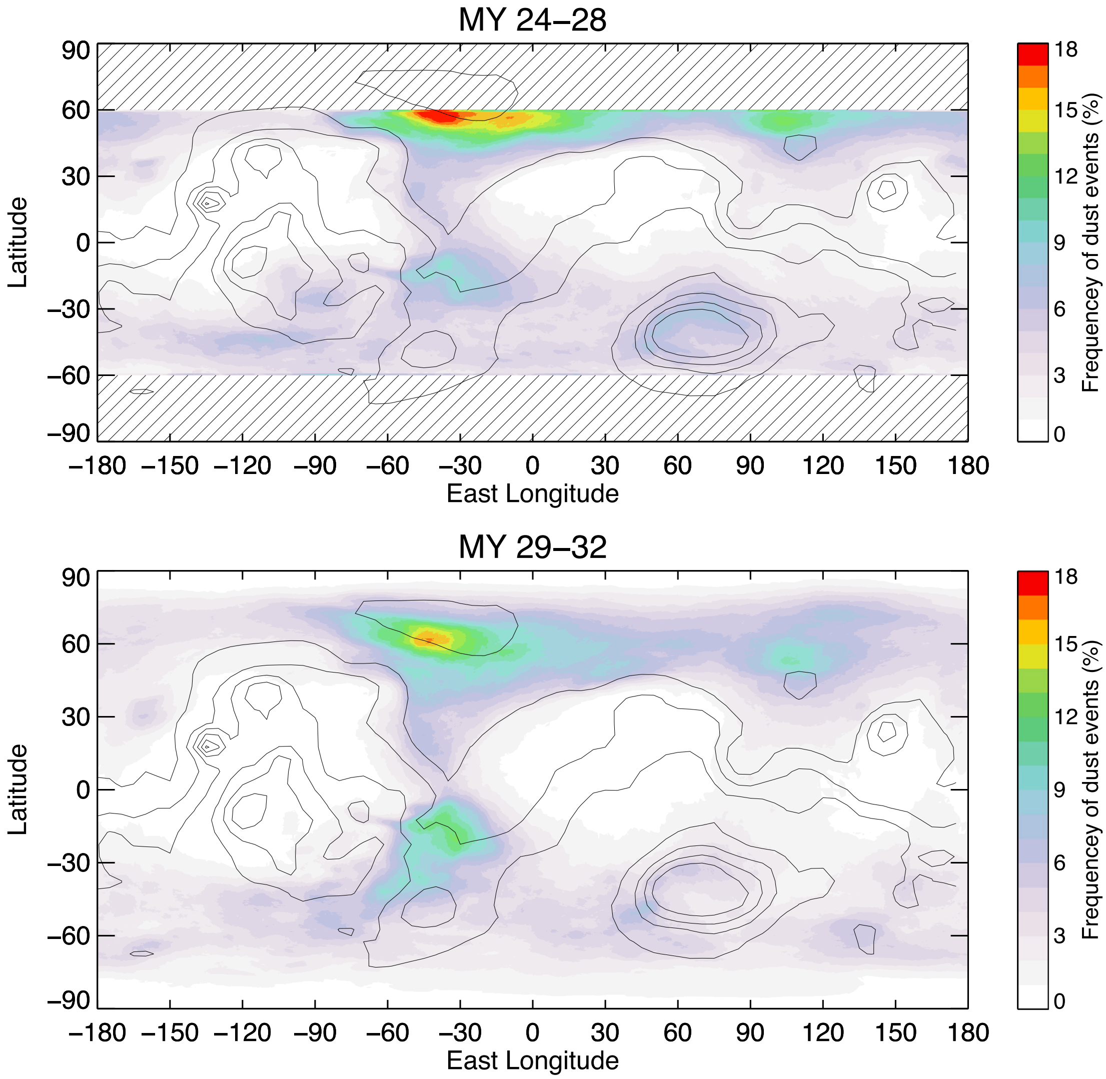

Fig. 4. Dust storm instance occurrence frequency map for MY 24–28 MOC MDGMs (top) and MY 29–32 MARCI MDGMs (bottom). Hatching indicates the bounds of the MOC equatorial MDGMs. Topography is shown in black contours every 2000 m. (For interpretation of the references to color in this figure legend, the reader is referred to the web version of this article.)

(Claritas Fossae) and equatorwards towards Syria Planum, where there is frequent, small single-sol dust storm activity. Next, along the northern rim of Hellas Basin at 30°S, 50–80°E, there exists a narrow band of increased storm instances, perhaps related to a cyclonic gyre in Hellas due to vertical elongation of parcels as they enter Hellas from the west, which is also noted in cloud cover in the same area around $L_s = 60°–150°$ (Kahre et al., 2020). At 30°N, 140°E, dust storm instances along the flanks of Elysium Mons may be forced by mesoscale circulations (Heavens et al., 2015). Finally, between 170–210°E and 30°N, dust activity is frequent in Arcadia and Amazonis Planitiae. These events may be related to mixed-layer rolls due to cold-air advection behind baroclinic waves (Heavens, 2017). Beyond these features at 30°N/S, the band of activity around 60°S may be explained in part by baroclinic wave activity in the southern hemisphere summer (Battalio et al., 2018) that does not form repeating, organized events. Each of these peaks are unrelated to sequence activity, as they are unorganized over multiple sols and do not travel from their origination regions.

Comparing the sizes of dust storm instances within sequences to non-sequence instances in Fig. 5. shows almost all of the larger instances belong to a sequence. Many smaller dust storm instances are part of sequences as well, but there are few large non-sequence instances. This is more quantitatively shown in Fig. 6, which provides the size distributions of sequence (top) and non-sequence (bottom) dust storm instances. Both distributions have an exponential decay with size ($R^2 > 0.99$), with fits of $y = (732.5 \pm 4.5)e^{(-0.1559\pm0.0015)x}$ for the sequence and $y = (5332.9 \pm 56.8)e^{(-0.878\pm0.020)x}$ for the non-sequence distributions. The decay rate is significantly smaller for the sequence instances. The top 1.1% of sequence-related dust storm instances are larger than 1.5×10^7 km^2, but the largest non-sequence storm instance is 1.28×10^7 km^2. The median size of the non-sequence instances is only 1.83×10^5 km^2, but the median sequence instance is roughly 5.7 times larger: 1.04×10^6 km^2. The mean size of sequence dust storm instances is 2.11×10^6 km^2, which is 5.5 times larger than the non-sequence instances (3.82×10^5 km^2). However, there are approximately 1.8 times more individual non-sequence dust storm sequences (9,872) than sequence instances (5,102), demonstrating that while sequences account for the largest individual events, they are less frequent than unorganized storm instances.

A third important difference between non-sequence and sequence members is the lifetime of their members. Fig. 7 shows the distributions of the duration (in sols) for sequence (top) and non-sequence (bottom) members. (Note that here we refer to “members” as opposed to “instances” because instances are individual dust storms on a single

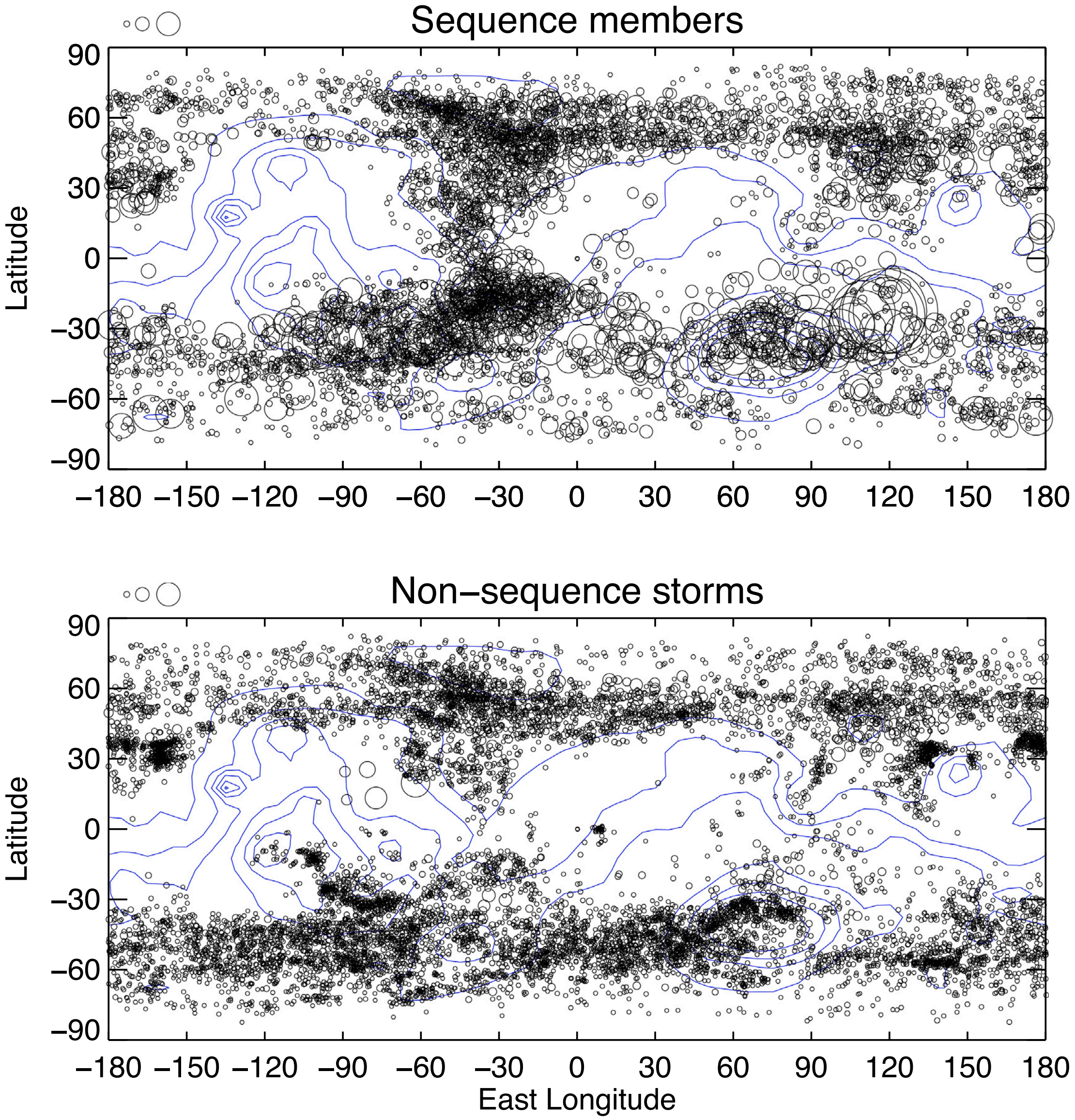

Fig. 5. Latitude–longitude distribution of dust storm instance centroids for sequence instances (top) and non-sequence instances (bottom). Each circle indicates a single instance on a single sol and is scaled by storm area. Legends at the top of each panel indicate the sizes of instances: 10^6, 5×10^6, and 10^7 km^2. Blue contours indicate topography in 2000 m increments. (For interpretation of the references to color in this figure legend, the reader is referred to the web version of this article.)

sol, while members refer to the lifetime of dust storms over several sols.) The distributions decay exponentially ($R^2 > 0.999$), with fits of $y = (545.9 \pm 2.6)e^{(-0.4230 \pm 0.0036)x}$ for the sequence and $y = (4212.3 \pm 19.5)e^{(-1.136 \pm 0.013)x}$ for the non-sequence distributions. Again, the distribution for sequence members decays significantly more slowly. The median duration for a sequence member is 2 sols, with a mean duration of 3.3 sols, and the median duration for non-sequence members is 1 sols, with a mean of 1.6 sols. The dust storm sequence is somewhat comparable to the "regional" dust storm of Cantor et al. (2001), defined as larger than 1.6×10^6 km^2 and longer than 2 sols; however, while the duration of sequences is comparable to "regional" storms, the definition of a sequence is not dependent on size explicitly. Thus, in these three ways—spatial, size, and duration distributions—dust storm instances that belong to a sequence are distinct from those that do not.

3.1.4. Sequence paths

Fig. 8 shows the paths that sequences take, plotted on the median MDGM for MY 29. This figure is an improvement over Wang and Richardson (2015) in that the MDAD is longer duration, includes sequences of duration as short as 3 sols, and includes circumpolar sequences. Sequences in the northern hemisphere follow more coherent tracks. Storms routinely travel around the polar cap edge, with 49 traveling from Acidalia towards Utopia, for example. Storms that deviate from the circumpolar track enter Acidalia, Utopia, and Arcadia Planitia in the ratio 59:32:17 or roughly 4:2:1. A smaller percentage of these events continue southwards (see Section 3.1.5). Upon reaching the southern hemisphere, Acidalia sequences tend to turn towards Argyre Basin or Noachis Terra, and Utopia sequences usually travel towards Hellas Basin.

Sequence paths in the southern hemisphere are less organized than those in the northern hemisphere. A small number of sequences travel around the southern polar cap, with the majority traveling from west to east. A very small number travel from east to west, some following flushing events from the northern hemisphere. Two other organized tracks are aligned with 60°S: the Aonia–Solis–Valles Marineris track (Battalio and Wang, 2019) that intersects with the southern end

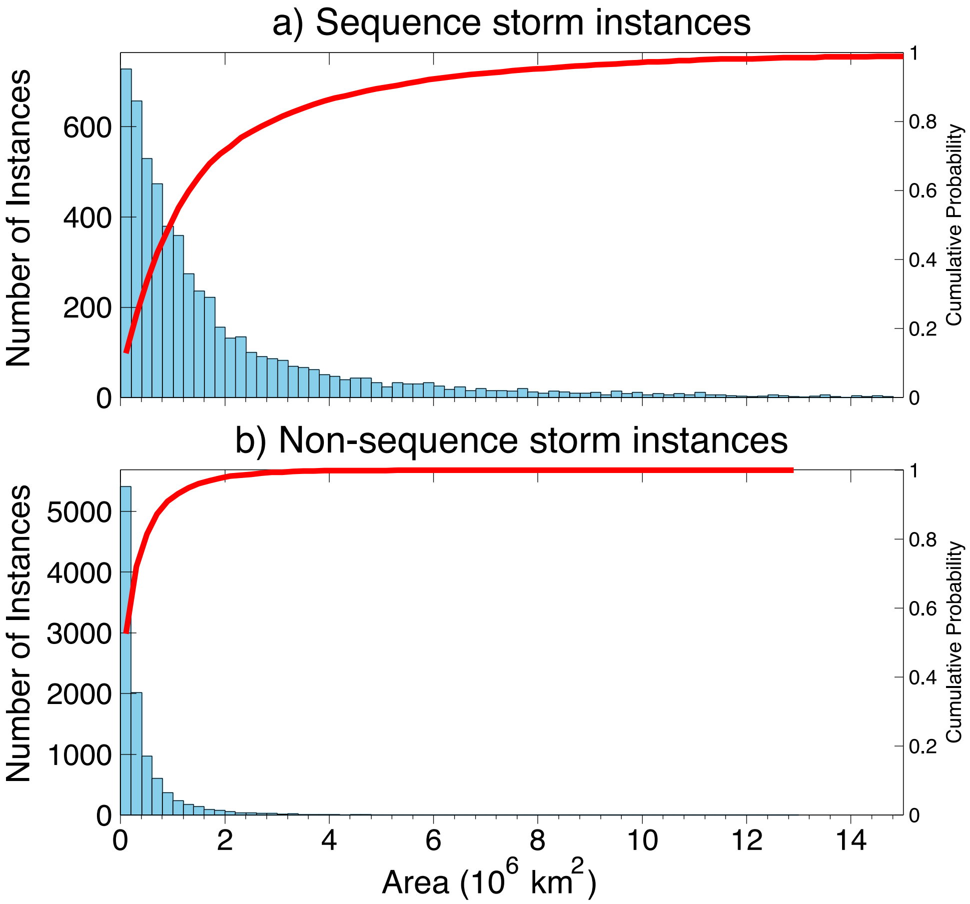

Fig. 6. Histograms of the areas of sequence dust storm instances (a) and non-sequence dust storm instances (b).

of the Acidalia track and a track progressing from Promethei Terra (on the eastern edge of Hellas), through Terra Cimmeria and either north into Elysium Planitia or east into Terra Sirenum.

3.1.5. *Flushing sequences*

For a sequence to be identified as flushing, it must travel more than 30 degrees in latitude from its origination area. Of the 133 sequences that meet this criterion, almost all do this by traveling from the polar caps towards or across the equator (Fig. 8). The most common pathways for a sequence to travel are through the northern hemisphere channels identified by Wang and Richardson (2015), but a large number (37% or 48) flush through the Aonia–Solis–Valles Marineris track (Battalio and Wang, 2019). A small minority of exceptions (4 sequences or 3%) flush poleward from near the equator. This behavior is exhibited by two sequences that develop near Xanthe Terra (as opposed to originating further north in Chryse or Acidalia) and travel southward and two sequences in Amazonis Planitia and travel north.

As noted in Fig. 8, in the northern hemisphere, the Acidalia track is the most traveled, followed by the Utopia and Arcadia tracks. Supplemental Figure 3 shows the frequency map, made in the same manner as Fig. 4, of only the flushing sequences. The peak region of flushing sequences in Supplemental Fig. 3 is in Xanthe and Margaritifer Terras, as this is the confluence location of the Acidalia–Chryse track from the north and the Aonia–Solis–Valles Marineris track from the south. The ratio of Acidalia to Utopia to Arcadia flushing events from Supplemental Table 1 is 41:22:11, or approximately 4:2:1, which updates a ratio from Wang and Richardson (2015) of 3:1:1. The updated result includes shorter duration sequences and a longer record of MDGMs. The updated ratio of flushing events is the same as the number of sequences that enter each channel from the circumpolar track, indicating that perhaps the number of seed events may partly control the amount of activity that flushes through each channel.

A further subtype of the flushing sequence is the turning sequence. This type of sequence is relatively rare (14 sequences). The turning behavior occurs when an Acidalia sequence turns usually to the east (9 sequences) and grows towards Noachis Terra after crossing the equator; however, in three instances, a sequence (*r06-2*, *s11-1*, and *B07-1*) turned west towards Aonia. Two sequences (*r06-2* and *B11-1*) traveling from Utopia turned to the west towards Noachis Terra. Interestingly, turning sequences are not distributed evenly across years. Four are in MY 27, and three are in MY 31. Ten come in pairs—one almost immediately after the other. This suggests that the specific global-scale dynamic conditions required for turning are relatively rare but can last for many tens of sols.

3.2. *Classification of sequences by growth curves*

We now more carefully investigate the lifecycles of sequences. Three main groups of sequences are identified by their growth curves. Growth curves show how the area and number of members change over the lifetime of the sequence. Fig. 9 shows the growth curves of sequences that exemplify each category. For each panel, the thick, black line shows the total area of the sequence on a particular sol. Individual sequence members are plotted by thinner, colored lines. Dashed lines show when two or more members combine. The legend at the top left identifies each member and gives the total number of members. There are roughly equal numbers of sequences in each group. The classification of each sequence is given in Supplemental Table 1.

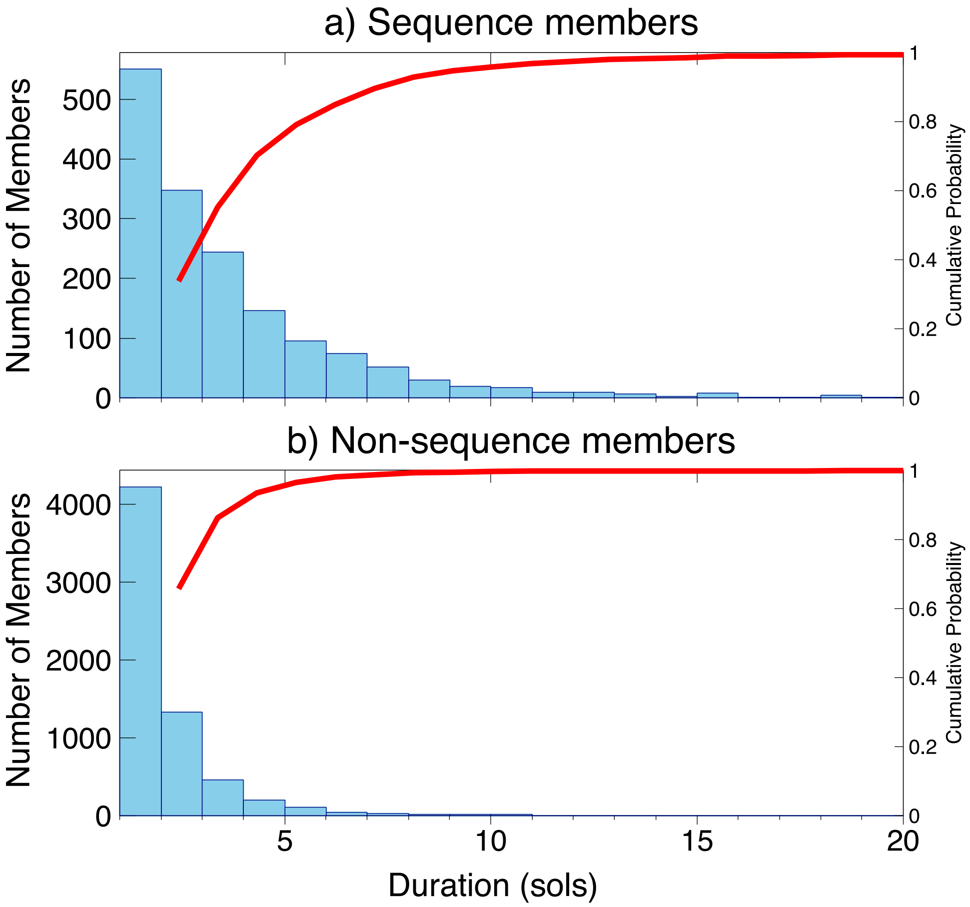

Fig. 7. Histograms of the duration of sequence members (a) and non-sequence members (b).

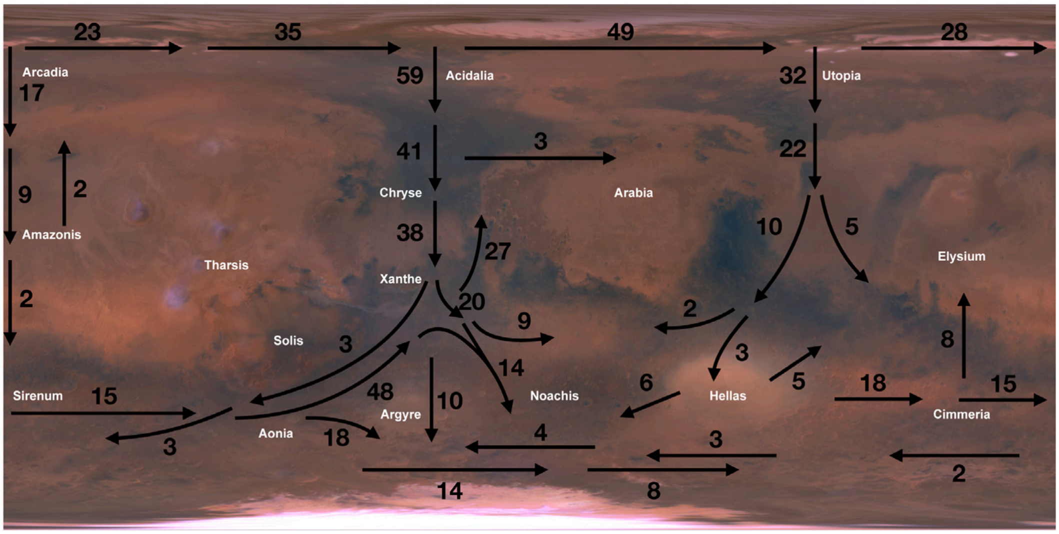

Fig. 8. Paths of dust storm sequences observed during MY 24–32 plotted on the median MDGM for MY 29 in a simple cylindrical map projection. The number of sequences traveling along each path is indicated.

The “Main Member” sequence is distinguished by a single prominent member that lasts for the majority of the sequence and has a maximum area at least double the maximum area of any other member. There are 69 Main Member sequences. An example, *B02-2*, is shown in Fig. 9a from MY 29 in the Aonia–Solis–Valles Marineris storm track. Member *B02_011* lasts the entire duration of the sequence and is more than double the size of the other seven members, though two members combine with the original member. With an average duration

a.) Main Member

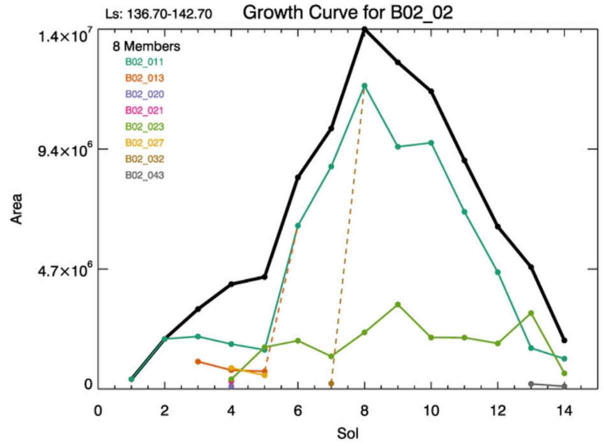

b.) Continuous Development

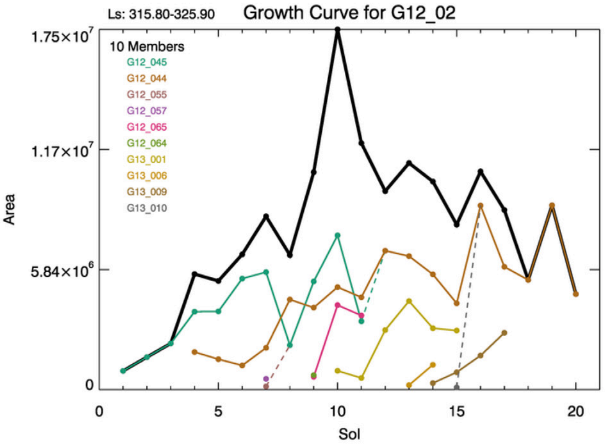

c.) Sequential Redevelopment

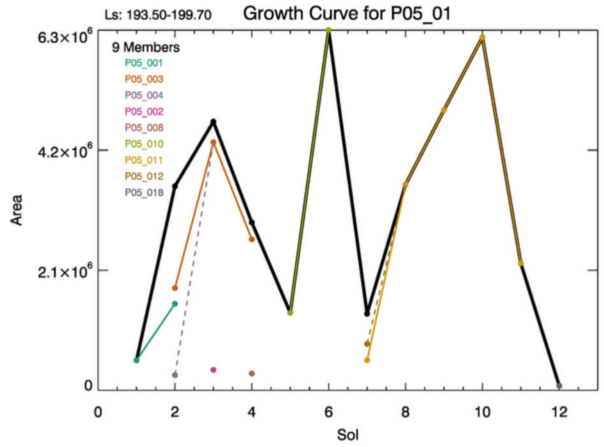

Fig. 9. Growth curves for the three types of sequences identified: Main Member (a), Continuous Development (b), and Sequential Redevelopment (c). For each plot, the total sequence area on each sol is shown in the thick, black line. Individual sequence members are shown as thinner lines colored by the legend on the left. Dashed lines show when two members combine. The L_s range is indicated at top left. Note: the ranges of the x- and y-axes change for each subpanel.

of 10.43 sols, Main Member sequences tend to be shorter than other classes. Their average area is 3.19 × 10^6 km^2. The average number of members within a Main Member sequences is also the fewest (5.11 members/sequence). Fourteen sequences have only one member. However, the average duration of the constituent members is the longest at 4.12 sols, or 48.5% of the duration of the whole sequence. Most main member sequences involve flushing towards or crossing the equator (68.7%). These statistics are summarized in Supplemental Table 2.

“Continuous Development” sequences are characterized by large numbers of members, none of which grow more than 50% larger than the other members (Fig. 9b). On any given sol, there are one or more moderately sized dust storm instances. Continuous Development sequences have repeating dust activity with few or no lulls in activity; i.e., once this type of sequences begins, it continues with new members starting as old members decay until the sequence ends. Many members may initiate, grow, and subside during the sequence, but the total sequence either remains steady in area or only grows because additional overlapping members are added to the sequence. There are 51 Continuous Development sequences. An archetype for this class is sequence *G12-2*, which flushes through Acidalia after the winter solstice in MY 30 (Fig. 9b). The lifetime of the sequence is shown in Supplemental Fig. 1. Ten members compose the sequence, and while member *G12_044* lasts almost the entirety of the sequence, it never grows over 20% larger than the other members, preventing it from being a Main Member sequence. The sequence attains its maximum area halfway through its lifetime at Sol 10 by adding members, not because any single member attains dominance. This sequence type is related to but not the same as “consecutive dust storm” classification of Wang and Richardson (2015), which was based on sequence trajectories. Thus, Continuous Development sequences usually exhibit repeating activity over the same area, but this is not always the case, though the total area of coverage over the lifetime of the sequence of the Continuous Development is the largest at 1.01 × 10^7 km^2. These sequences tend to be the longest in duration (15.9 sols) and have the most number of members (12.11 members/sequence). The individual members are medium in duration (3.39 sols), yet last for a shorter percentage of the sequence duration (27.3%) than Main Member sequences.

There are 54 “Sequential Redevelopment” sequences that have multiple medium to large members and several to many small members. The large members have a maximum area 50% larger than the smaller members, but no single large member is dominant in duration or area from the other large members. The large members grow and decay in succession such that two members are not concurrently growing, while smaller members can grow and decay spontaneously. The growth curve for the entire sequence has multiple peaks where each individual large member experiences an entire cycle of development. The growth curve of the archetypal Sequential Redevelopment sequence, *P05-1*, is shown in Fig. 9c. It is a pre-solstice flushing sequence in the Acidalia track in MY 28. Composed of nine members, this sequence has three dominant members (*P05_003*, *P05_010*, and *P05_011*), each of which are approximately double the area of the other six members. Sequential Redevelopment sequences are related to the “sequential activation dust storms” of Wang and Richardson (2015), as many of these sequences exhibit pulses of activity with each member advancing the whole sequence forward. These sequences tend to be of roughly equal duration (15.7 sols) to the Continuous Development class. Due to the pulsing nature of the members, the duration of the average member is the smallest of all classes at 3.3 sols or only 23.2% of the lifetime of the average sequence. Because this class of sequence is composed of both large and small members, the average member size is not large (1.22 × 10^6 km^2).

Finally, a fourth group of sequences does not easily fit into the three classes discussed above. Many of these sequences (54 in total) share characteristics of two of the three classes. For example, several sequences exhibit Continuous Development character but have a short-lived member with a maximum area that falls between the 50% and 200% cutoffs for storms in the Main Member and Sequential Redevelopment sequences.

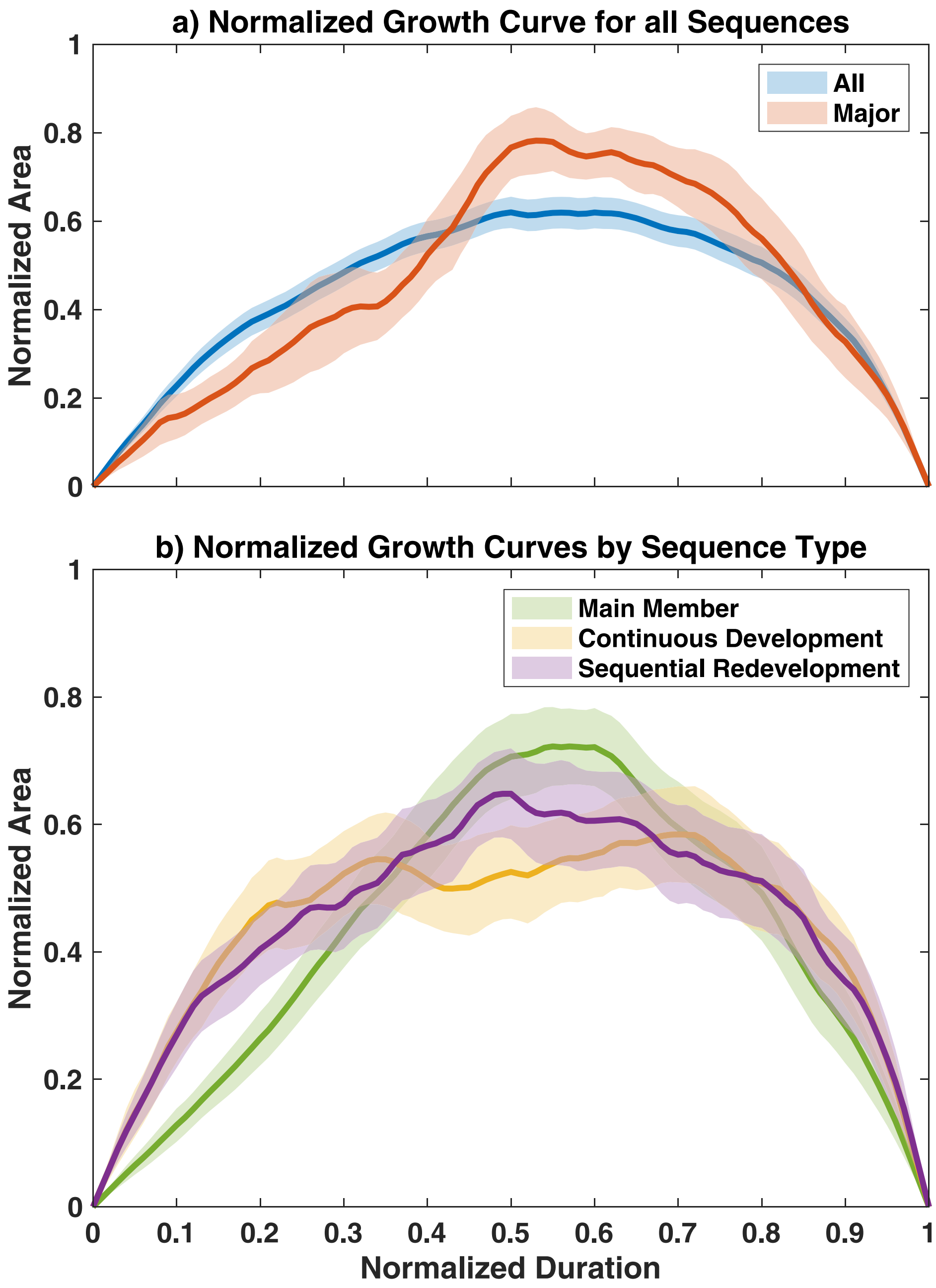

Fig. 10. The normalized growth rates for all sequences and only major sequences (a), and the normalized growth curves for the Main Member, Continuous Development, and Sequential Redevelopment sequence classes (b). The dark, thick lines show the mean, and the shaded areas indicate the 95% confidence bounds. (For interpretation of the references to color in this figure legend, the reader is referred to the web version of this article.)

To directly compare the sequence classes, Fig. 10 compiles all of the growth curves to calculate the normalized growth rates of the classes. To combine the sequences, each growth curve is normalized by the maximum area and duration of the sequence. The thick, dark lines are the average growth curve, and the shaded areas are the 95% confidence bounds. The Continuous Development class (Fig. 10b, yellow) reaches a moderately steady plateau and maintains that value throughout its lifetime due to the steady generation of dust storm area over the lifetime of the sequence class. For the Continuous Development sequences, the relative peaks in area occur 35% and 75% through the sequence duration. The Sequential Redevelopment class (Fig. 10b, purple) is initially similar to that of the Continuous Development class with a period of rapid growth but is then followed by slower growth instead of plateauing due to more and more members being added to the sequence. The peak area of this class occurs halfway through the normalized duration. The Continuous Development and Sequential Redevelopment classes have steep initial growth rates, 1.1×10^6 km^2/sol and 9.6×10^5 km^2/sol over the first two sols, respectively, because they often grow by multiple members simultaneously. The Main Member (Fig. 10b, green) curve is different, with an initial growth rate that is almost linear (approximately 8.5×10^5 km^2/sol for the first 4 sols) and is dominated by the growth and decay of the primary member. The average peak area of this class occurs almost 60% through the lifetime of the sequence class. The average normalized growth curve (Fig. 10a, blue) of all sequences is similar to half a sine curve, slightly skewed towards 1. It is an amalgamation of the three classifications and the non-classified sequences and so has large initial growth rates and a rapid decay with a peak around the midpoint of the normalized

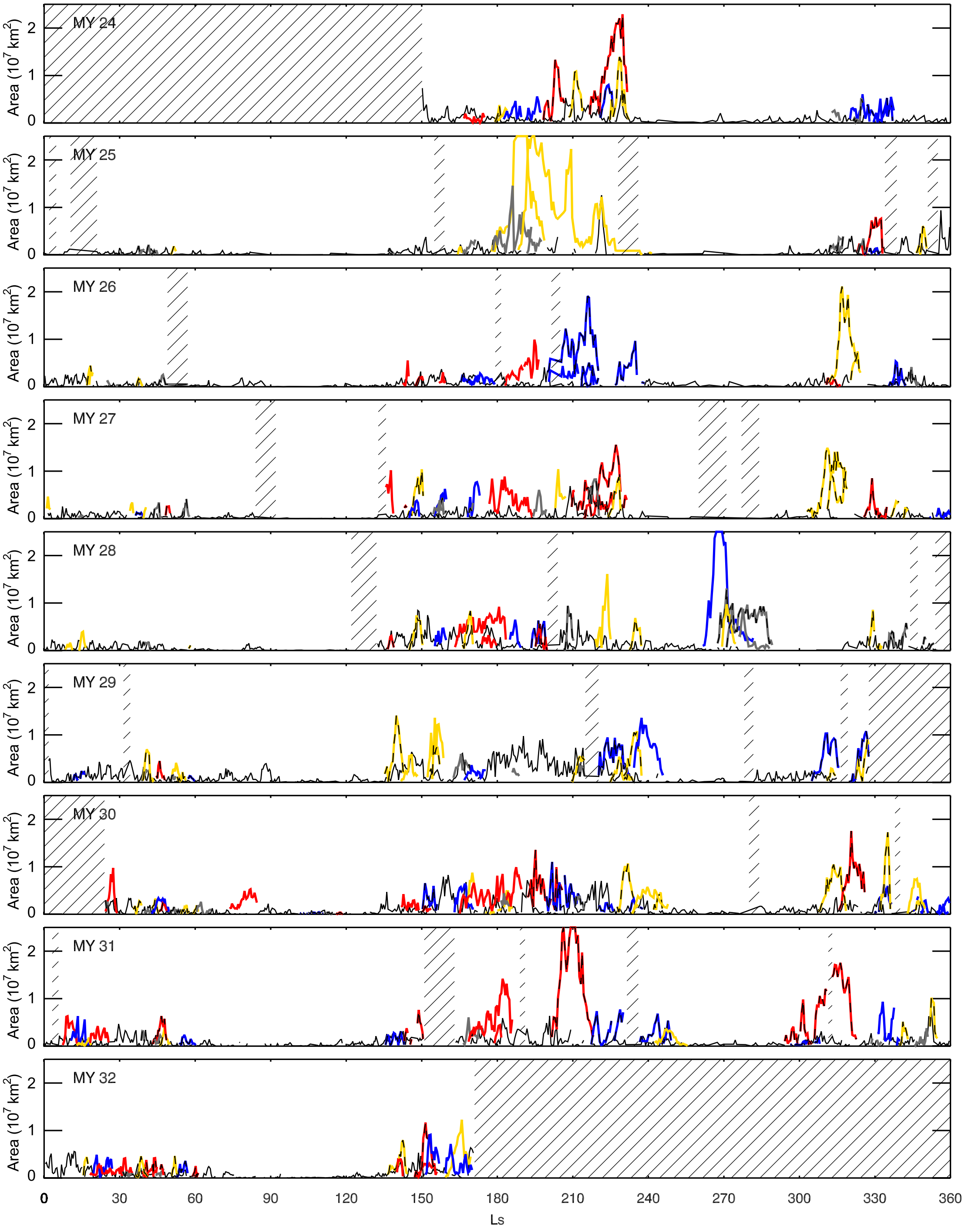

Fig. 11. Sequence areas as a function of L_s for the Main Member (gold), Sequential Redevelopment (blue), Continuous Development (red), and other (gray) sequences. Non-sequence dust storm instance areas are shown in a thin black line. Flushing sequences are indicated with dashed lines. Periods when MDGMs are missing are indicated with hatching. (For interpretation of the references to color in this figure legend, the reader is referred to the web version of this article.)

lifetime. It is notable that the decay rate of sequences is faster than that of the growth rates; however, this may be dependent on the confidence level used in selecting dust storm instances.

With these classifications, we can evaluate the climatology of sequences. Fig. 11 shows areas of dust activity with time for each year, effectively plotting every sequence growth curve in a continuous plot. Sequences are colored by classification: gold for Main Member, blue for Sequential Redevelopment, red for Continuous Development, and gray for other. The thin black line shows the area of non-sequence storm activity summed on each sol. Dashed lines within the sequences show those that are flushing. Hatching indicates missing MDGMs. The typical dust storm season stands out, but the most active period with the largest sequences can be narrowed down to the L_s = 140°–250° period. This corresponds to the period of partial overlap of the Aonia–Solis–Valles Marineris season (L_s = 120°–180°) (Battalio and Wang, 2019) and the pre-solstice peak (L_s = 170°–250°) associated with the A events (Kass et al., 2016). A secondary season corresponds to the C events during L_s = 300°–360°. Finally, there is a tertiary season between L_s = 10°–70°

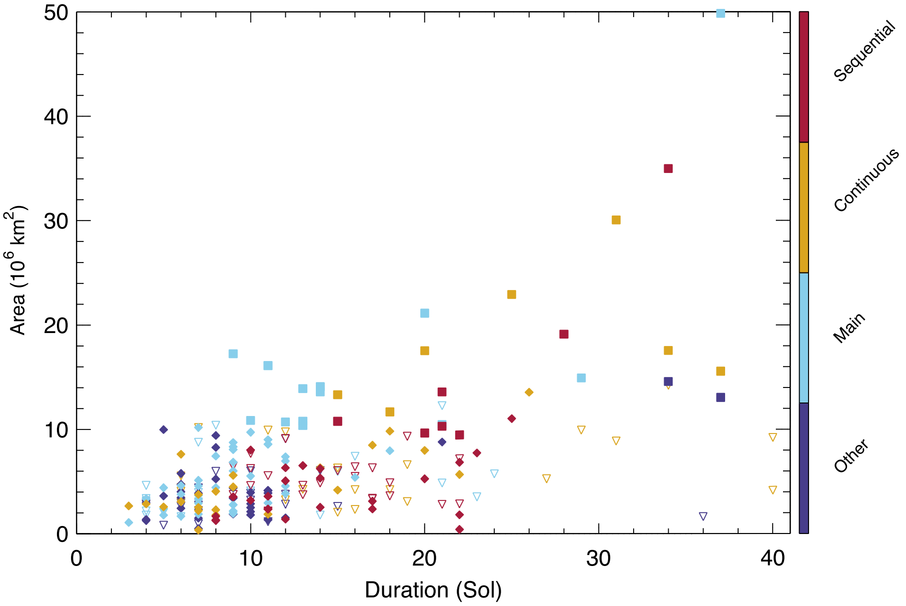

Fig. 12. Scatterplot of sequence duration vs maximum sequence area. Points are colored by sequence classification. Squares indicate major sequences, diamonds indicate flushing minor sequences, and open triangles indicate non-flushing minor sequences. (For interpretation of the references to color in this figure legend, the reader is referred to the web version of this article.)

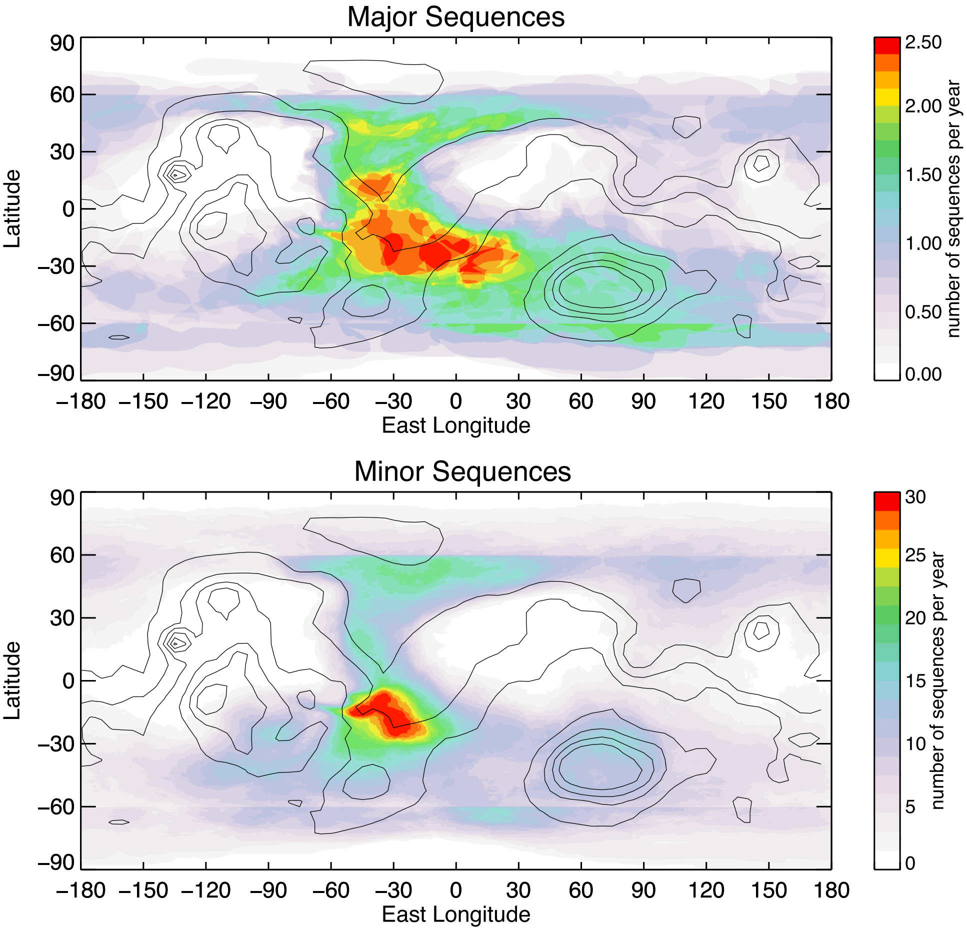

Fig. 13. Occurrence map for the number of major sequences per Mars year (top) and the number of minor sequences per Mars year (bottom). Topography is indicated with black contours every 2000 m. (For interpretation of the references to color in this figure legend, the reader is referred to the web version of this article.)

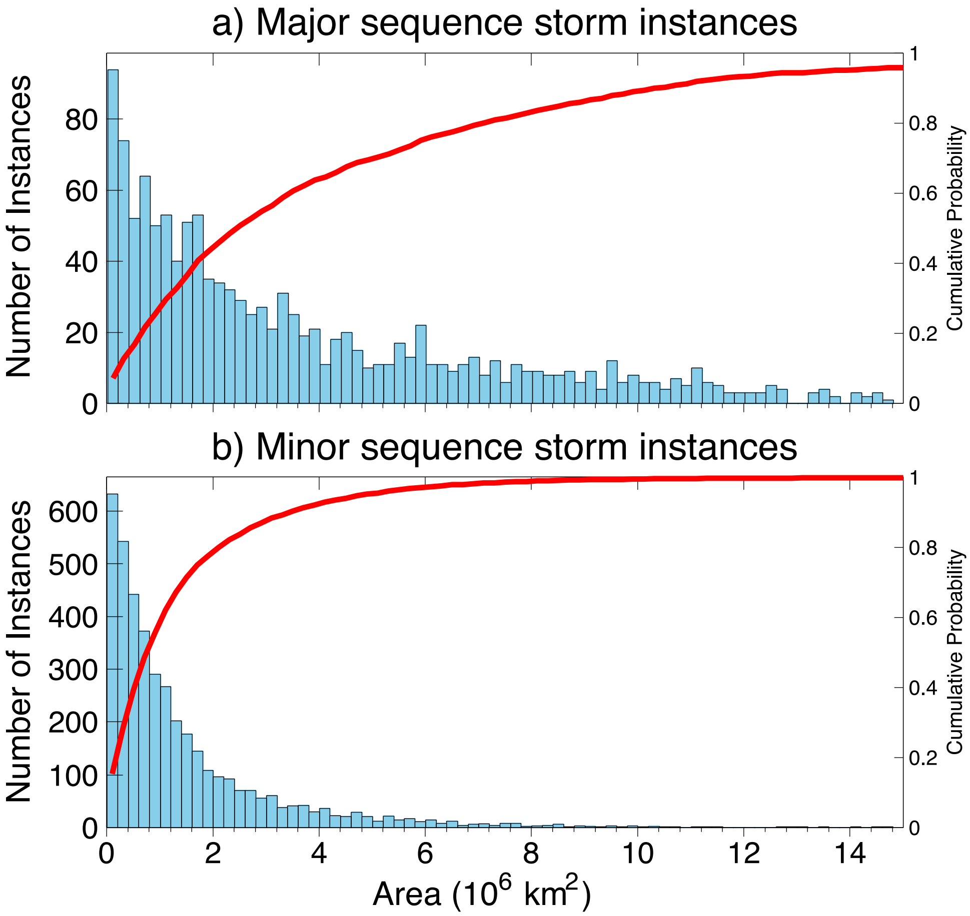

Fig. 14. Histograms of the areas of major (a) and minor (b) sequence dust storm instances.

due to the pre-solstice Aonia–Solis–Valles Marineris track. There is no apparent seasonality in the class of sequence, but the Main Member and Sequential Redevelopment classes exhibit flushing behavior more often than the Continuous Development class, though there are examples of flushing in all categories, including in the unclassified group.

3.3. Major and minor sequences

Finally, we examine differences in sequences based on their size and impact to global opacity. Fig. 12 shows a scatterplot of dust sequence duration versus maximum sequence area. Color indicates the class of sequence. The general trend is that the longer the sequence duration, the larger the maximum area. Most sequences remain below approximately 10^7 km^2; however, a small number grow larger. We separate sequences by size into “Major” ($>10^7$ km^2) and “Minor” ($<10^7$ km^2) sequences. We further discriminate the 43 sequences $>10^7$ km^2 by comparing the change in global opacity after the sequences ends and on whether they are flushing sequences. Only those flushing sequences that demonstrate an increase in the zonal-mean opacity above 0.3 are included (contours in Fig. 2). This eliminates 12 sequences that are $>10^7$ km^2. The areas, durations, locations, classes, number of members, and relationship to the Kass et al. (2016) classification scheme for each major sequence are presented in Table 1. Many major sequences are associated with dust events that are initiated in the northern hemisphere by baroclinic eddies, flush through one of the three dominant channels, and spawn large regions of dust lifting in the southern hemisphere. These events precipitate the A and C temperature perturbations of Kass et al. (2016). Additional major sequences are involved with the MY 25 and MY 28 global dust events (noted GDE in Table 1), and 4 sequences result from the Aonia–Solis–Valles Marineris storm track (noted ASV in Table 1). There are only 5 instances of a major sequence not associated with one of these storm types. However, in those 5 cases, they are flushing sequences similar to the A and C events that increased the global opacity yet are not the largest of that season. Note, B-type events are composed of storm instances that are small in area and confined to the southern hemisphere polar region so cannot cause a major sequence.

The seasonality of major sequences is more constrained than that of the entire sequence catalog. Major sequences are shown in Fig. 2 in gold. Major sequences initiate between L_s = 198°–242° and last no later than L_s = 249° in northern hemisphere fall and initiate between L_s = 303°–332° and last until L_s = 340° in northern hemisphere winter, with the exception of the GDE and ASV cases. The tighter bounds on the timing of major sequences versus the A and C events listed in Kass et al. (2016) and the column dust optical depth as shown in Fig. 2 from Montabone et al. (2015) are because the A and C events are defined from temperature perturbations that can last much longer than the discrete dust sequences that cause rises in global opacity. The longest duration major sequence is 71 sols during the MY 25 GDE; the longest non-GDE major sequence is *s06-1* that lasts 35 sols. The average major sequence duration is 19 sols, which is longer than any defined class of sequences described in Section 3.2. However, the average number of members (8) of a major sequence is not much different from the number of members of the minor sequences (7). There is a preference for major sequences to be Main Member (15 sequences) over the Continuous Development (7) and Sequential Redevelopment (7) types, but this may be due to a limited sample size.

The locations of major sequences are shown in Fig. 13. The number of sequences and sequence members is calculated in a similar way to

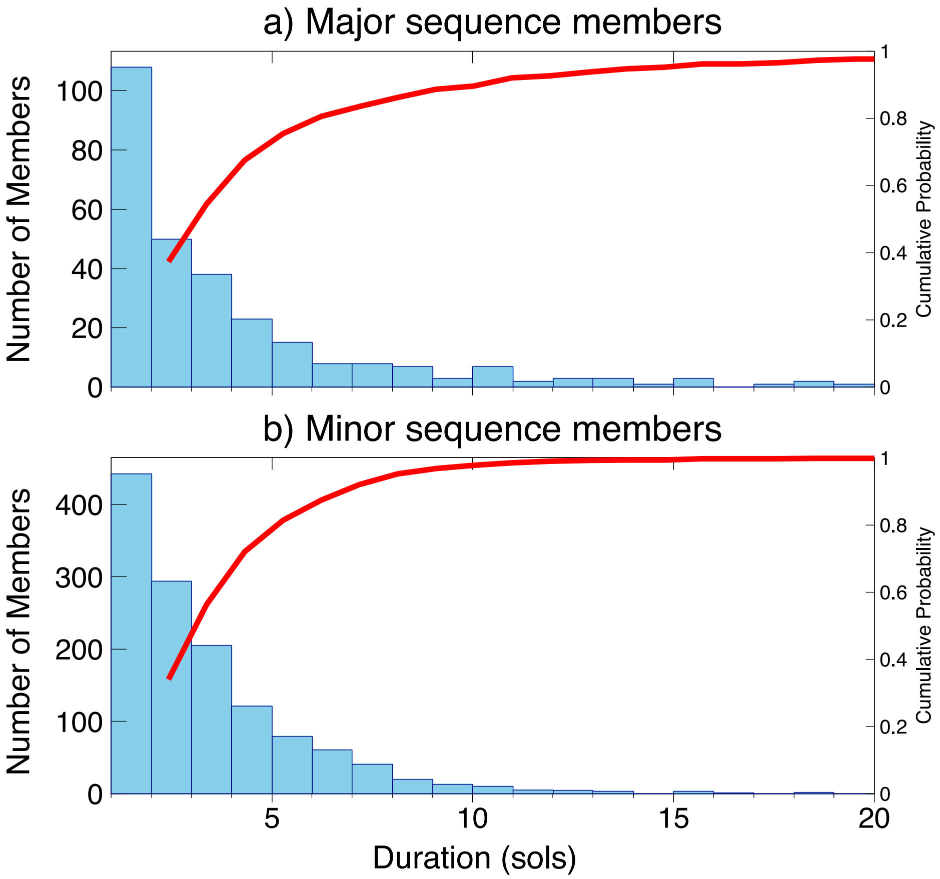

Fig. 15. Histograms of the duration of major (a) and minor (b) sequence members.

Fig. 4 by normalizing by number of sequences per year. Most major and minor sequences are found in the Acidalia track, and from Table 1, there are only 7 non-GDE major sequences not associated in some way with the Acidalia–Chryse/ASV track. From Fig. 13, major dust storm sequences spawn closer to the equator than minor sequences, with little frequency poleward of 60°. The reason for this partly stems from the seasonality of major sequences. As noted previously, major sequences associated with the A and C events have a tighter bound on their seasonality immediately before and after the solstitial pause of transient waves, when wave activity is closer to the equator (Lewis et al., 2016). Transient wave activity with closer proximity to the equator facilitates flushing into the southern hemisphere, which allows for further growth of the dust event (Wang, 2018). It should be noted that defining major events by changes in zonal-mean opacity and maximum area may preferentially select sequences that flush, as high-latitude sequences are by necessity smaller in area and induce zonal-mean opacity changes that may occur in regions with missing data.

To demonstrate that major sequences are distinct and unique from minor sequences, we show two main discriminators between types: size of individual dust storm instances and the duration of sequence members. The number of members per sequence does not appreciably change for major and minor sequences, as mentioned previously. The most consistent discriminator between major and minor sequences is the distribution of the area of the constituent dust storm instances, as shown in Fig. 14. The distribution of the area of minor sequence dust storm instances (Fig. 14b) drops off rapidly with a fit of $y = (632.5 \pm 4.0)e^{(-0.182\pm0.002)x}$ at $R^2 > 0.99$, similar to the distribution of all sequence dust storm instances shown in Fig. 6a. The collection of major sequence dust instances samples the larger instances from the total sequence instance distribution; thus, the distribution falls off more slowly with increasing size, with a fit of $y = (73.7 \pm 1.4)e^{(-0.068\pm0.002)x}$ at $R^2 > 0.95$. The median area of dust storm instances from major sequences is almost three times as large (2.45×10^6 km^2) as that of minor sequence instances (8.33×10^5 km^2). So, major sequences are larger than minor sequences by having a higher percentage of larger dust storm instances and because the maximum instance size is larger. A second difference between major and minor sequences is in the duration of their members. Again, the distributions of member duration decay exponentially for minor sequences (Fig. 15b), with a fit of $y = (445.1\pm3.4)e^{(-0.413\pm0.006)x}$ at $R^2 > 0.999$, similarly to how the distribution behaves for all sequences (Fig. 7a). However, for major sequences, the tail of the duration distribution is much longer (Fig. 15a), though the distribution is still well-fit ($R^2 > 0.98$) by an exponential: $y = (103.0 \pm 1.8)e^{(-0.540\pm0.018)x}$. This difference is due to longer sequences having longer members as shown in Section 3.2 and because of the relationship between maximum sequence size and duration as shown in Fig. 12. Finally, we note that the normalized growth rate of major sequences is different from that of all sequences (Fig. 10a). Major sequences initially grow more slowly, then approximately halfway through their normalized duration experience a surge of activity.

In discriminating between minor and major sequences, we seek to examine why some are minor sequences and others are major by comparing the dust storm activity over the 10 sols immediately previous to the start of minor and major sequences. Fig. 16 displays the average dust storm activity area for the 10 sols before major (a) and minor (b) sequences for the hemisphere in which the sequences originate. The blue line is the average, with the 95% confidence bounds shown; the red line is the median storm activity area. Sols where the values on respective sols are different at 99% (95%) confidence are indicated with filled (open) circles. Periods before major sequences

Table 1

Major sequences. Sols refers to the duration of the sequence. Class can be "continuous", "sequential", "main", or "other" (see Section 3.2). Type can be "flushing", "turning", "GDE" for Global Dust Event, or "non" for non-flushing (see Section 3.1.5). Region refers to location of sequence origination. "K16 class" refers to type according to Kass et al. (2016) (A, B, or C) or if it belonged to the Aonia–Solis–Valles Marineris track (Battalio and Wang, 2019), or a global event.

Seq ID	MY	Start L_s	End L_s	sols	# of Mems	Max Area (10^6 km^2)	Class	Type	Region	K16 class
m07–1	24	198.3	206.6	15	6	13.32	Continuous	Flushing	North	
m07–2	24	208.4	213.7	10	5	10.87	Main	Flushing	Acidalia	
m08–1	24	216.8	231.6	25	21	22.91	Continuous	Turning	Acidalia	A
m08–3	24	224.8	232.2	13	14	13.91	Main	Flushing	Arcadia	A
e05–1	25	177.8	198.7	37	11	49.83	Main	GDE	South	GDE
e05–2	25	178.3	197.5	34	26	14.56	Other	GDE	North	GDE
e06–1	25	188.4	241.4	71	9	27.45	Main	GDE	South	GDE
r06–2	26	199.9	220.1	36	15	19.10	Sequential	Flushing	Utopia	A
r07–3	26	226.8	239.8	20	10	9.66	Sequential	Turning	Acidalia	
r12–2	26	311.9	323.2	20	7	21.11	Main	Turning	Acidalia	C
s02–2	27	144.5	150.5	13	12	10.39	Main	Flushing	ASV	ASV
s06–1	27	209.6	231.4	37	18	15.55	Continuous	Flushing	Acidalia	A
s11–1	27	303.0	319.0	29	7	14.90	Main	Turning	Acidalia	C
s11–2	27	311.1	318.4	14	7	14.10	Main	Turning	Acidalia	C
P06–1	28	219.0	225.0	11	3	16.12	Main	Non	Hellas	A
P08–1	28	261.6	281.6	34	12	34.97	Sequential	GDE	Acidalia	GDE
P08–2	28	267.5	289.2	37	3	13.04	Other	Turning	Acidalia	GDE
B02–2	29	136.7	142.7	14	8	14.07	Main	Flushing	ASV	ASV
B03–1	29	152.3	158.6	14	10	13.6	Main	Non	Cimmeria	ASV
B07–1	29	220.3	232.5	22	5	9.46	Sequential	Flushing	Acidalia	A
B07–2	29	230.2	237.3	13	8	10.78	Main	Flushing	Acidalia	A
B07–4	29	234.3	246.1	21	16	13.59	Sequential	Non	ASV	A
B11–1	29	304.9	315.9	21	7	10.31	Sequential	Flushing	Utopia	C
B12–1	29	320.1	327.5	15	12	10.78	Sequential	Flushing	Arcadia	
G07–3	30	227.6	234.2	12	1	10.71	One	Flushing	Acidalia	A
G12–1	30	307.6	318.5	21	6	10.47	Main	Flushing	Acidalia	C
G12–2	30	315.8	325.9	20	10	17.52	Continuous	Flushing	Acidalia	C
G13–2	30	332.1	336.1	9	4	17.24	Main	Flushing	Utopia	
D06–1	31	201.3	218.4	31	9	30.05	Continuous	Flushing	Utopia	A
D11–3	31	303.7	322.6	34	22	17.54	Continuous	Turning	Acidalia	C
F03–3	32	147.2	155.5	18	13	11.68	Continuous	Flushing	ASV	ASV

have larger median and average dust activity areas in the 10 sols prior to their initiation than minor sequences. Between −6 and −1 sols, the differences are significant at 95%, and between −4 and −1, the differences are significant at 99%. Additionally, there is an increase in storm activity area in the lead-up to a major sequence, but with minor sequences, there is no significant trend in storm activity areas from −10 sols to −1 sol. The trend in the mean dust activity area of sols before major sequences using only those sols that are significantly different than minor sols (i.e., only those indicated with circles in Fig. 16) is $4.7\pm0.1\times10^5$ km^2/sol, which is significant at 99% confidence. The trend line (black) with its associated 95% confidence interval (blue, dashed curves) is also shown in Fig. 16. Thus, major sequences generally occur after unorganized storm activity or other sequences and rarely occur without precursor dust events, with increasing average activity areas within 6 sols of their initiation.

The size distribution of these dust storm instances in these 10 sols is shown in Fig. 17, for dust storm instances before a major sequence (a) and instances before a minor sequence (b). Immediately before a minor sequence, dust instance area is small. The median instance area is only 5.8×10^5 km^2, with a distribution that drops rapidly after the median. Only 37.7% of dust instances are larger than 10^6 km^2, with no instances larger than 1.4×10^7 km^2. For the period before a major sequence, the median instance area is 2.2×10^6 km^2, with a long-tailed distribution. This indicates that in the 10 sols before a major sequence, storm activity is distinct from that preceding a minor sequence.

4. Summary and discussion

Eight Mars years (MY) of Mars Daily Global Maps (MDGMs) are analyzed to generate the Mars Dust Activity Database (MDAD), which covers MY 24, L_s = 150° to MY 32, L_s = 171°. There are 14,974 dust storm instances compiled into 7,827 dust storm members. Dust storm members are multi-sol dust events that have a lifetime that can be tracked from one sol to the next. Unorganized dust storm activity is found mostly along the polar ice caps in the northern and southern hemispheres during their respective fall to spring seasons (Fig. 2). Collections of organized dust storm members are called dust storm sequences, an example of which is shown in Fig. 1. Sequences in this dataset are composed of one or more members that follow a general trajectory and have a lifetime of at least three sols. The size distribution of both sequence and non-sequence dust storm instances follows an exponential decay with area, but the size distribution of unorganized dust storm instances decays much more rapidly (Fig. 6), meaning that dust storm instances involved with a sequence are generally larger. The smooth size distributions indicate that evolution from local, to regional, and to global-scale dust events may be a continuous process, as the existence of independent growth processes may manifest as discontinuities in the dust activity size distribution (Cantor et al., 2001). Additionally, members involved in a sequence have a longer duration than those not contained in a sequence (Fig. 7). The seasonality of sequences is similar to that of unorganized activity, but some sequences in late fall or early winter in each hemisphere can travel from the polar regions towards the equator through topographic channels south of Acidalia, Utopia, and Arcadia Planitiae in the northern hemisphere and north of the Argyre region in the southern hemisphere (Figs. 4 and 8). There are three seasons of flushing activity. The primary season from L_s = 140°–250° corresponds to a period of partial overlap between the southern hemisphere winter season and the northern hemisphere fall flushing season. A secondary period occurs in the northern hemisphere winter season during L_s = 300°–360°, and a less active southern hemisphere fall period occurs from L_s = 10°–70°.

Sequences are further classified into three types: Main Member, Continuous Development, and Sequential Redevelopment. Growth curves for archetypes of these classes are shown in Fig. 9. Main

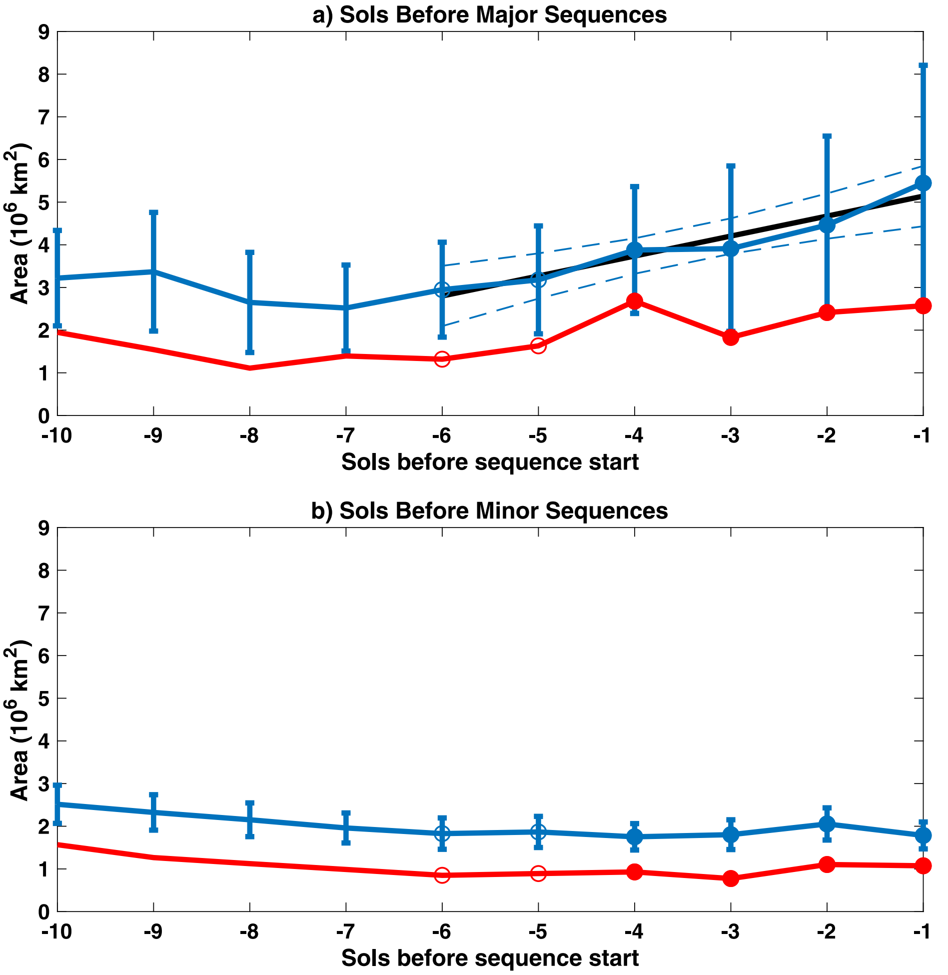

Fig. 16. Averaged dust storm activity area in the originating hemisphere for the 10 sols preceding major (a) and minor (b) sequences. The blue line shows the average activity area with the standard error indicated. The red line shows the median activity area for each sol. Sols where the major versus minor values are statistically different at 99% (95%) confidence are plotted with filled (open) circles. The black solid line shows the linear fit to the significant values of the pre-major averages with the 95% confidence intervals for the fit dashed in blue. (For interpretation of the references to color in this figure legend, the reader is referred to the web version of this article.)

Member sequences are composed of one or more members, one of which generates the majority of dust area covered. Main Member sequences tend to be the shortest-lasting at only 10.56 sols. Continuous development sequences have a large number of constituent members, none of which grows more than 50% larger than any other member. Continuous development sequences tend to be the longest in duration (15.9 sols) and the largest in average area (1.01×10^7 km^2). Sequential Redevelopment sequences exhibit pulses of activity during their lifetime, whereby individual members consecutively grow 50% larger than other concurrent members. This class of sequence has the smallest average constituent members (1.22×10^6 km^2). A remaining group cannot be easily classified, usually because they exhibit characteristics of two of the described classes.

Independent of the classification scheme, larger sequences can influence the global opacity and are designated “Major” sequences. These sequences must have a maximum single sol area of $>10^7$ km^2, flush, and must instigate a region of zonal-mean opacity at 9.3 μm of at least 0.3. Major sequences are usually associated with the “A” and “C” temperature signatures of Kass et al. (2016), the Aonia–Solis–Valles Marineris dust storm track (Battalio and Wang, 2019), or a global dust event. Major dust sequences are distinct from minor sequences by the sizes of the constituent members—double the median minor sequence member area—and by the duration of these members.

Dust activity immediately before major and minor sequences is distinct. In the 6 sols leading to a major sequence, the total area of dust activity is significantly larger than that before minor sequences, with a median area of 2.2×10^6 km^2. In the 6 sols before the beginning of a major sequence there is a significant trend of increasing dust storm area of $4.7 \pm 0.1 \times 10^5$ km^2/sol. There is no such trend in the ten sols before a minor sequence (Fig. 16), with a dust area distribution that has a median of 5.8×10^5 km^2. Thus, major sequences appear to occur after the atmosphere has been already activated with precursor dust storm activity. The necessity of both long duration and large dust coverage area in changing the regional environment was demonstrated in the modeling efforts of Toigo et al. (2018). They showed that there is a threshold in impact on the atmosphere between storms that are 10^5 km^2 and 10^6 km^2 in area. The temporal threshold for impacts on the atmosphere for storms greater than 10^6 km^2 was found to occur around 10 sols. These temporal and spatial scales are largely supported by the results presented here.

Though the MDAD is the most comprehensive catalog of dust activity available, the single local time observing approach achieved with polar orbiters has drawbacks in developing a dust storm climatology. First, MDGMs generally capture only a single instant each sol, meaning any dust storms that decay before or initiate after the observation time may be missed. Second, while storm motion can be roughly deduced from one sol to the next, the exact path between MDGMs is not clear. A more comprehensive dust activity database is only achievable with additional polar orbiters or with areostationary observations, which would allow for near-continuous dust storm

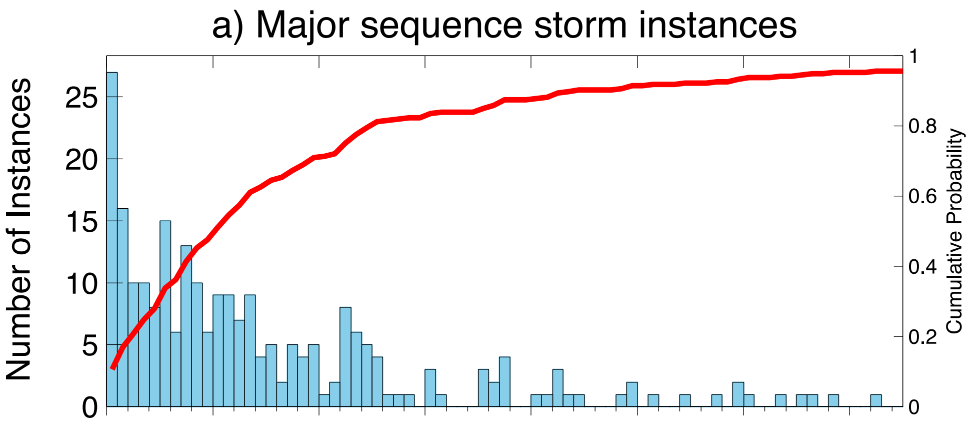
a) Major sequence storm instances

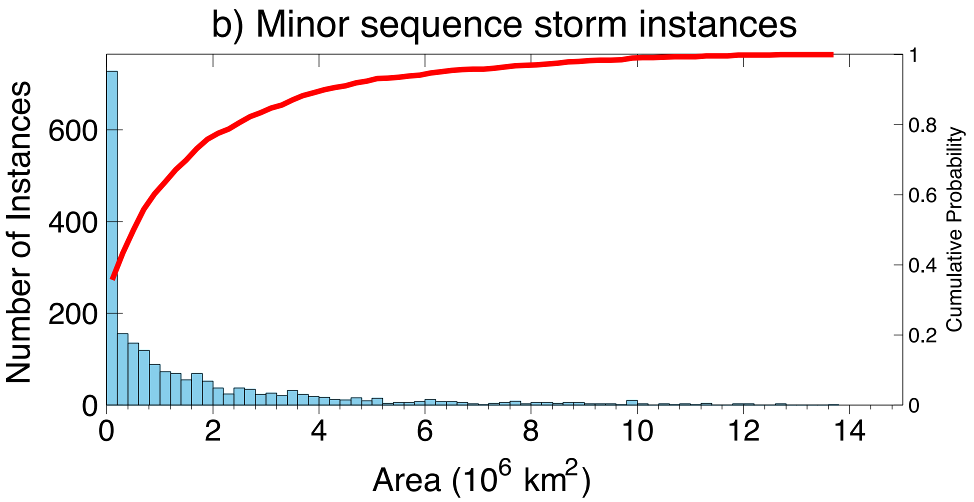
b) Minor sequence storm instances

Fig. 17. Histograms of the areas of pre-major sequence dust storm instances contained in Fig. 16a (a) and areas of pre-minor sequence instances contained in Fig. 16b (b).

monitoring. The effort required to manually detect dust storm activity on daily maps can be prohibitive; thus, for the sake of expediency, dust databases derived from areostationary observations will demand artificial intelligence (e.g., Gichu and Ogohara, 2019).

Future work will expand the length of the Mars Dust Activity Database to the present, determine if the location of activity determines the synoptic impacts on the atmosphere, and assess the predictive capabilities of trends in dust storm area preceding major sequences.

Acknowledgments

The Mars Dust Activity Database can be found at <https://doi.org/10.7910/DVN/F8R2JX>. MGS MOC MDGMs are available at <https://doi.org/10.7910/DVN/WWRT1V>. Version 1 MRO MARCI MDGM is available at <https://doi.org/10.7910/DVN/G2VENZ>. Version 2 MRO MARCI MDGM is available at <https://astrogeology.usgs.gov/search/map/Mars/MarsReconnaissanceOrbiter/MARCI/MARS-MRO-MARCI-Mars-Daily-Global-Maps>. The gridded column dust optical depth data of Montabone et al. (2015) are available at <http://www-mars.lmd.jussieu.fr/mars/dust_climatology/>. We thank Luca Montabone and R. John Wilson for reviewing and improving the manuscript. This work is supported by NASA PDART Grant NNX16AG47G and NASA MDAP Grant 80NSSC17K0475.

Appendix A. Supplementary data

Supplementary material related to this article can be found online at https://doi.org/10.1016/j.icarus.2020.114059.

References

Barnes, J.R., Haberle, R.M., Wilson, R.J., Lewis, S.R., Murphy, J.R., Read, P.L., 2017. The global circulation. In: Haberle, R.M., Clancy, R.T., Forget, F., Smith, M.D., Zurek, R.W.E. (Eds.), The Atmosphere and Climate of Mars. In: Cambridge Planetary Science, Cambridge University Press, pp. 229–294. http://dx.doi.org/10.1017/9781139060172.009.

Battalio, M., Szunyogh, I., Lemmon, M., 2016. Energetics of the martian atmosphere using the Mars Analysis Correction Data Assimilation (MACDA) dataset. Icarus 276, 1–20. http://dx.doi.org/10.1016/j.icarus.2016.04.028.

Battalio, M., Szunyogh, I., Lemmon, M., 2018. Wave energetics of the southern hemisphere of Mars. Icarus 309, 220–240. http://dx.doi.org/10.1016/j.icarus.2018.03.015.

Battalio, M., Wang, H., 2019. The Aonia–Solis–Valles dust storm track in the southern hemisphere of Mars. Icarus 321, 367–378. http://dx.doi.org/10.1016/j.icarus.2018.10.026.

Battalio, M., Wang, H., 2020. Eddy evolution during large dust storms. Icarus 338, 113507. http://dx.doi.org/10.1016/j.icarus.2019.113507.

Cantor, B.A., 2007. MOC Observations of the 2001 Mars planet-encircling dust storm. Icarus 186 (1), 60–96. http://dx.doi.org/10.1016/j.icarus.2006.08.019.

Cantor, B.A., James, P.B., Caplinger, M., Wolff, M.J., 2001. Martian dust storms: 1999 Mars Orbiter Camera observations. J. Geophys. Res. 106 (E10), 23653–23687. http://dx.doi.org/10.1029/2000JE001310.

Gichu, R., Ogohara, K., 2019. Segmentation of dust storm areas on mars images using principal component analysis and neural network. Prog. Earth Planet. Sci. 6 (1), 1–12. http://dx.doi.org/10.1186/s40645-019-0266-1.

Guzewich, S.D., Toigo, A.D., Kulowski, L., Wang, H., 2015. Mars Orbiter Camera climatology of textured dust storms. Icarus 258, 1–13. http://dx.doi.org/10.1016/j.icarus.2015.06.023.

Guzewich, S.D., Toigo, A.D., Wang, H., 2017. An investigation of dust storms observed with the Mars Color Imager. Icarus 289, 199–213. http://dx.doi.org/10.1016/j.icarus.2017.02.020.

Haberle, R.M., Juárez, M.d.l.T., Kahre, M.A., Kass, D.M., Barnes, J.R., Hollingsworth, J.L., Harri, A.M., Kahanpää, H., 2018. Detection of Northern

Hemisphere transient eddies at Gale Crater Mars. Icarus 307, 150–160. http://dx.doi.org/10.1016/j.icarus.2018.02.013.

Haberle, R.M., Pollack, J.B., Barnes, J.R., Zurek, R.W., Leovy, C.B., Murphy, J.R., Lee, H., Schaeffer, J., 1993. Mars atmospheric dynamics as simulated by the NASA ames general circulation model 1. The zonal-mean circulation. J. Geophys. Res. 98, 3093–3124. http://dx.doi.org/10.1029/92JE02946.

Heavens, N.G., 2017. Textured dust storm activity in Northeast Amazonis–Southwest Arcadia, Mars: Phenomenology and dynamical interpretation. J. Atmos. Sci. 74 (4), 1011–1037. http://dx.doi.org/10.1175/JAS-D-16-0211.1.

Heavens, N.G., Cantor, B.A., Hayne, P.O., Kleinböhl, A., McCleese, D.J., Piqueux, S., Schofield, J.T., Shirley, J.H., 2015. Extreme detached dust layers near Martian volcanoes: Evidence for dust transport by mesoscale circulations forced by high topography. Geophys. Res. Lett. 42, 7623–7932. http://dx.doi.org/10.1002/2015GL063354.Received.

Hinson, D.P., Wang, H., Smith, M.D., 2012. A multi-year survey of dynamics near the surface in the northern hemisphere of Mars: Short-period baroclinic waves and dust storms. Icarus 219 (1), 307–320. http://dx.doi.org/10.1016/j.icarus.2012.03.001.

Hollingsworth, J.L., Barnes, J.R., 1996. Forced stationary planetary waves in Mars's winter atmosphere. J. Atmos. Sci. 53 (3), 428–448. http://dx.doi.org/10.1175/1520-0469(1996)053<0428:FSPWIM>2.0.CO;2.

Kahre, M., Haberle, R., Hollingsworth, J., Wolff, M., 2020. MARCI-Observed clouds in the Hellas Basin during northern hemisphere summer on Mars: Interpretation with the NASA/Ames Legacy Mars Global Climate Model. Icarus 338 (113512), http://dx.doi.org/10.1016/j.icarus.2019.113512.

Kass, D.M., Kleinböhl, A., McCleese, D.J., Schofield, J.T., Smith, M.D., 2016. Interannual similarity in the martian atmosphere during the dust storm season. Geophys. Res. Lett. 43, http://dx.doi.org/10.1002/2016GL068978.

Kulowski, L., Wang, H., Toigo, A.D., 2017. The seasonal and spatial distribution of textured dust storms observed by Mars Global Surveyor Mars Orbiter Camera. Adv. Space Res. 59 (2), 715–721. http://dx.doi.org/10.1016/j.asr.2016.10.028.

Lewis, S.R., Mulholland, D.P., Read, P.L., Montabone, L., Wilson, R.J., Smith, M.D., 2016. The solsticial pause on Mars: 1. A planetary wave reanalysis. Icarus 264, 456–464. http://dx.doi.org/10.1016/j.icarus.2015.08.039.

Martin, L.J., Zurek, R.W., 1993. An analysis of the history of dust activity on Mars. J. Geophys. Res. 98 (E2), 3221–3246. http://dx.doi.org/10.1029/92JE02937.

Montabone, L., Forget, F., Millour, E., Wilson, R.J., Lewis, S.R., Cantor, B.A., Kass, D.M., Kleinböhl, A., Lemmon, M.T., Smith, M.D., Wolff, M.J., 2015. Eight-year Climatology of Dust Optical Depth on Mars. Icarus 251, 65–95. http://dx.doi.org/10.1016/j.icarus.2014.12.034.

Mooring, T.A., Wilson, R., 2015. Transient eddies in the MACDA Mars reanalysis. J. Geophys. Res.: Planets 120, 1–26. http://dx.doi.org/10.1002/2015JE004824.

Mulholland, D.P., Lewis, S.R., Read, P.L., Madeleine, J.-B., Forget, F., 2016. The solsticial pause on Mars: 2 modelling and investigation of causes. Icarus 264, 465–477. http://dx.doi.org/10.1016/j.icarus.2015.08.038.

Strausberg, M.J., Wang, H., Richardson, M.I., Ewald, S.P., Toigo, A.D., 2005. Observations of the initiation and evolution of the 2001 Mars global dust storm. J. Geophys. Res.: Planets 110 (E2), E02006. http://dx.doi.org/10.1029/2004JE002361.

Toigo, A.D., Richardson, M.I., Wang, H., Guzewich, S.D., Newman, C.E., 2018. The cascade from local to global dust storms on Mars: Temporal and spatial thresholds on thermal and dynamical feedback. Icarus 302, 514–536. http://dx.doi.org/10.1016/j.icarus.2017.11.032.

Wang, H., 2007. Dust storms originating in the northern hemisphere during the third mapping year of Mars Global Surveyor. Icarus 189 (2), 325–343. http://dx.doi.org/10.1016/j.icarus.2007.01.014.

Wang, H., 2018. Cross-equatorial flushing dust storms and northern hemisphere transient eddies: An analysis for mars year 24. J. Geophys. Res.: Planets 123 (7), 1732–1745. http://dx.doi.org/10.1029/2018JE005623.

Wang, H., Ingersoll, A.P., 2002. Martian clouds observed by Mars Global Surveyor Mars Orbiter Camera. J. Geophys. Res. 107 (E10), 5078. http://dx.doi.org/10.1029/2001JE001815.

Wang, H., Richardson, M.I., 2015. The origin, evolution, and trajectory of large dust storms on Mars during Mars years 24–30 (1999–2011). Icarus 251, 112–127. http://dx.doi.org/10.1016/j.icarus.2013.10.033.

Wang, H., Richardson, M.I., Toigo, A.D., Newman, C.E., 2013. Zonal wavenumber three traveling waves in the northern hemisphere of Mars simulated with a general circulation model. Icarus 223 (2), 654–676. http://dx.doi.org/10.1016/j.icarus.2013.01.004.

Wang, H., Richardson, M.I., Wilson, R.J., Ingersoll, A.P., Toigo, A.D., Zurek, R.W., 2003. Cyclones, tides, and the origin of a cross-equatorial dust storm on mars. Geophys. Res. Lett. 30 (9), 1488. http://dx.doi.org/10.1029/2002GL016828.